

Evidence for a kilometre-scale seismically slow layer atop the core-mantle boundary from normal modes

Stuart Russell^{1,2}, Jessica C.E. Irving³, Lisanne Jagt¹, Sanne Cottaar¹

¹University of Cambridge

²Universität Münster

³University of Bristol

Key Points:

- Normal mode centre frequencies are a sensitive data type to detect seismically anomalous thin layers at the core-mantle boundary.
- A slow and dense layer on the order of 1 km thick atop the core-mantle boundary can improve the fit to normal mode data.
- The inclusion of a layer is likely not a unique way to improve the 1D model and layer properties remain uncertain.

Plain language summary

Normal modes are long-period oscillations of the whole Earth as it vibrates after large earthquakes. The frequency that a mode oscillates at depends on the interior structure of the Earth. Research suggests a global and thin layer of anomalous composition and low seismic wave speeds may have formed at the base of Earth's mantle, but would be difficult to observe seismically. We test and quantify the effect of this layer on the frequencies at which normal modes vibrate. We then compare these predictions to a large dataset of normal mode frequency measurements to examine whether such a layer is consistent with observed data. We find that not only is a layer of 1 - 3 km thickness permitted by the modes, but that a layer being present improves the fit to the data. There are a wide range of parameters that adequately fit the dataset so we cannot be specific about its properties. Furthermore a layer is likely not a unique way to improve the model. A seismically slow layer at the core-mantle boundary has implications for processes in the mantle and outer core and the interaction between them.

Abstract

Geodynamic modelling and seismic studies have highlighted the possibility that a thin layer of low seismic velocities, potentially molten, may sit atop the core-mantle boundary but has thus far eluded detection. In this study we employ normal modes, an independent data type to body waves, to assess the visibility of a seismically slow layer atop the core-mantle boundary to normal mode centre frequencies. Using forward modelling and a dataset of 353 normal mode observations we find that some centre frequencies are sensitive to one-dimensional kilometre-scale structure at the core-mantle boundary. Furthermore, a global slow and dense layer 1 - 3 km thick is better-fitting than no layer. The well-fitting parameter space is broad with a wide range of possible seismic parameters, which precludes inferring a possible composition or phase. Our methodology cannot uniquely detect a layer in the Earth but one should be considered possible and accounted for in future studies.

1 Introduction

The Earth's core-mantle boundary (CMB) is a major internal boundary in the planet, separating the liquid iron outer core from the solid silicate mantle. Structures and processes at the CMB affect convection in both the mantle and the outer core, with consequences for plate tectonics and the geomagnetic field. The lowermost mantle immediately atop the CMB is extremely complex; it contains numerous structures identified from seismology including ultra-low velocity zones (ULVZs).

ULVZs are extreme seismic anomalies tens of kilometres thick and hundreds of kilometres in diameter that exhibit velocity reductions on the order of 10% and 30% for P and S waves, respectively (e.g. Yu & Garnero, 2018). There are several possible origins of ULVZs including iron-enrichment (e.g. Wicks et al., 2010; Dobrosavljevic et al., 2019), the presence of melt or partial melt (e.g. Q. Williams & Garnero, 1996; Yuan & Romanowicz, 2017), or both combined (Liu et al., 2016; Dannberg et al., 2021). Melt of any origin in the lowermost mantle is expected to be dense (Boukaré et al., 2015) and should drain from the ULVZ under gravity (Hernlund & Tackley, 2007; Dannberg et al., 2021). If drainage occurs then ULVZs are expected to be accompanied by an extensive fully-molten layer which may have important implications for geochemical observations (e.g. Coltice et al., 2011) and for electromagnetic coupling between the core and mantle (e.g. Buffett et al., 2002; Holme & De Viron, 2013).

Body waves are commonly used to study ULVZs, including reflected phases (e.g. Brown et al., 2015), transmitted phases (e.g. Zou et al., 2007) and diffracted phases (e.g. Rost & Garnero, 2006; Li et al., 2022). Despite body waves being sensitive to ULVZs, they may not be sensitive to an accompanying layer if it is too thin. Travel times of $\text{PKKP}_{\text{diff}}$ relative to PKKP_{bc} are sensitive to and consistent with a thin layer on the order of kilometres thick, but show significant scatter impeding a conclusion on whether a layer exists or not (Russell et al., 2022).

In contrast to body waves, normal modes are very long-period free oscillations of the Earth excited after large earthquakes ($M_w \geq 7.4$). Normal modes appear as prominent peaks in the Fourier spectra of several days-long seismograms. The shape and frequencies of these peaks depend on the internal structure of the planet (e.g. Dziewonski & Gilbert, 1971; Dziewonski & Anderson, 1981). The degenerate frequencies that the mode would oscillate at in the absence of 3D structure, called centre frequencies, can be estimated from seismic spectra and give information about average 1D Earth structure. Constraining lateral heterogeneity requires study of spectra or the higher order coefficients of mode splitting functions (Woodhouse et al., 1986). Stoneley modes have peak sensitivity at the CMB interface (Stoneley, 1924; Koelemeijer et al., 2013). Splitting func-

tions can observe small-scale ULVZs if there is a long-wavelength component in their lateral distribution (Koelemeijer et al., 2012).

Building upon the results of Russell et al. (2022), we use forward modelling to test the sensitivity of normal mode centre frequencies to a kilometre-scale global low velocity layer atop the CMB. We then compare the modelling results to a dataset of centre frequency measurements to ascertain whether a globally layered CMB is compatible with seismic observations.

2 Data

Measuring centre frequencies of normal modes is non-trivial and the centre frequencies and splitting functions are calculated from spectra by inversion. We do not measure centre frequencies ourselves, but instead use published datasets. For this study we use the compilation used to construct the Elastic Parameters of the Outer Core (EPOC) model (Irving et al., 2018), together with Stoneley modes (Koelemeijer et al., 2013), the longest period modes (Deuss et al., 2011), and recently measured toroidal modes (Schneider & Deuss, 2021). This excludes inner-core sensitive modes, which may couple strongly due to unmodelled inner core anisotropy (Irving et al., 2008). Centre frequencies and measurement errors are taken from the most recent publication in which that mode is measured (Masters & Widmer, 1995; Resovsky & Ritzwoller, 1998; Widmer-Schmidrig, 2002; Deuss et al., 2013; Koelemeijer et al., 2013; Schneider & Deuss, 2021; REM, n.d.), giving a total of 353 modes. Centre frequencies are corrected for the first-order effects of Earth’s ellipticity (Dahlen & Tromp, 1998). A table of centre frequencies and errors can be found in Section S11.

3 Normal mode sensitivity to a layer

We use MINEOS (Woodhouse, 1988; Masters et al., 2011) to forward model the eigenfrequencies (centre frequencies) and eigenfunctions of the free oscillations of a given model. Slow and dense layers of different thicknesses are inserted above the CMB into a 1D model. This 1D model, referred to as EPOC, consists of PREM (Dziewonski & Anderson, 1981) for the mantle and inner core, while EPOC is used for the outer core as it improves the misfit for outer core sensitive modes.

We first investigate the sensitivity of the modes to the presence of a layer. The parameters for one test layer are -20% , -40% and $+50\%$ for δV_p , δV_s and $\delta \rho$ relative to PREM, respectively (absolute: 10.97 km s^{-1} , 4.36 km s^{-1} , 8.35 g cm^{-3}). As it has non-zero V_s we refer to this layer as the ‘solid layer’, however it could represent partial melt. We test a second layer with -33% , -100% and $+14\%$ for δV_p , δV_s and $\delta \rho$, respectively (absolute: 9.10 km s^{-1} , 0.00 km s^{-1} , 6.35 g cm^{-3}), and refer to this as the ‘molten layer’. This layer is identical to that explored by Russell et al. (2022) using PKKP diffracted waves.

Using the eigenfunctions from MINEOS we calculate sensitivity kernels (Dahlen & Tromp, 1998). Kernels are used to examine the sensitivity of a mode and to assess how sensitivity evolves as the model is varied. Figure 1 shows sensitivity kernels for ${}_3S_{26}$ and ${}_{15}S_{15}$ in the cases of EPOC, EPOC with a 10 km solid layer, and EPOC with a 10 km molten layer. For both modes, the sensitivity evolves when layers are included. ${}_3S_{26}$ shows a drastic change in character; it is a Stoneley mode in EPOC and for a molten layer, but not for a solid layer where the CMB sensitivity is reduced. The kernel for ${}_{15}S_{15}$ does not significantly change between different models, but does acquire a peak inside the solid layer. That sensitivity peaks in such thin regions validates the use of normal modes to study thin structures at the CMB, in contrast to their efficacy when investigating less extreme structures (e.g. Robson et al., 2022). Although we illustrate these extreme ex-

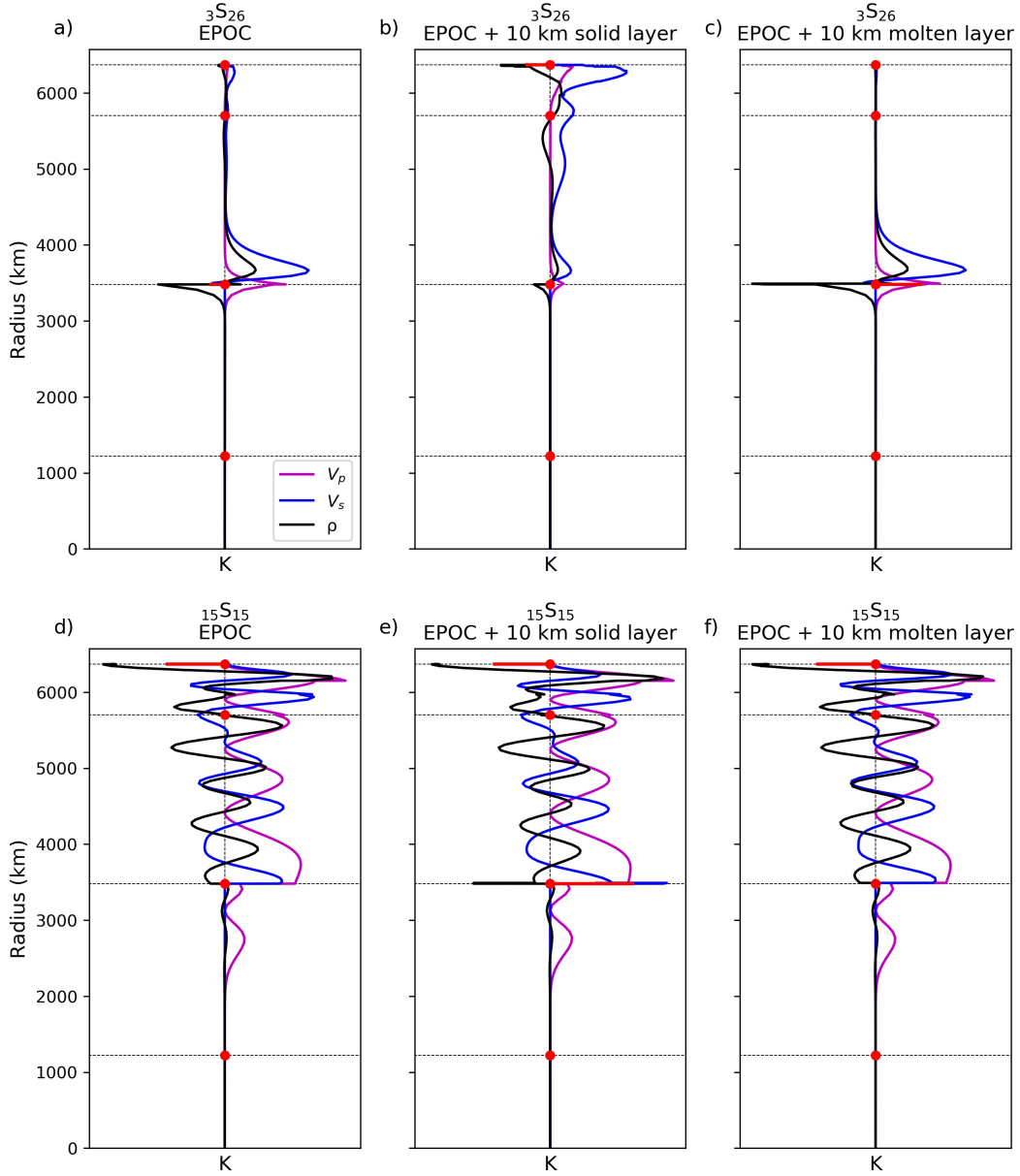


Figure 1. Sensitivity kernels, K , for two different modes in three different models indicated by subfigure titles, showing sensitivity to P-velocity (magenta), S-velocity (blue) and density (black). Horizontal dashed lines represent the major discontinuities: the surface, 660 km, CMB and ICB; and discontinuity sensitivity to displacement is given by red horizontal lines. Amplitudes are consistent across plots of the same mode.

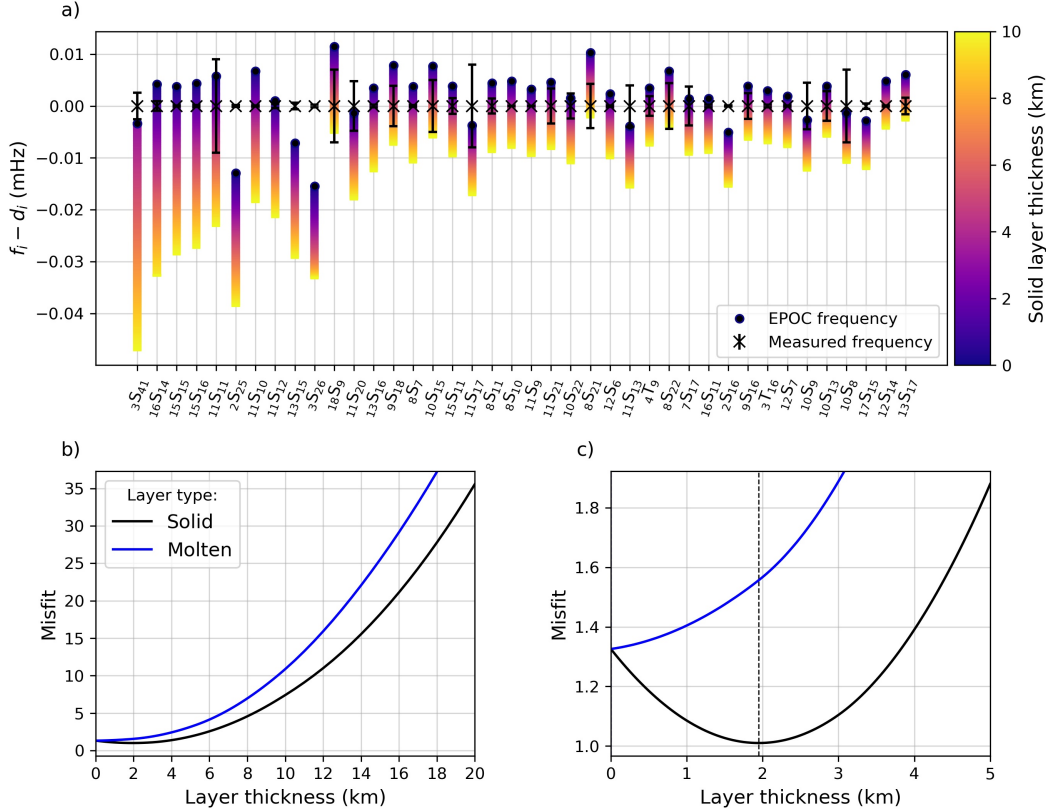


Figure 2. (a) Colours show eigenfrequencies predicted for different thicknesses of the solid layer, f_i , relative to the measured centre frequencies, d_i . Measurement errors, ϵ_d , are the black error bars. These are the 40 most sensitive modes ordered by the gradient of their eigenfrequencies with solid layer thickness. A plot showing (a) for all 353 modes used to calculate M can be found in Section S3. (b) and (c) show the misfit, M , as a function of layer thickness between 0 - 20 km and 0 - 5 km, respectively, for the solid (δV_p : -20%, δV_s : -40% and $\delta \rho$: +50%) and molten (δV_p : -33%, δV_s : -100% and $\delta \rho$: +14%) layers. The vertical dotted line marks the minimum in M for the solid layer.

amples, the majority of kernels do not notably change. Further sensitivity kernels are presented in Section S1.

Sensitivity kernels for the solid and molten layers often differ and this corresponds to drastic differences in behaviour of the eigenfrequencies as layer thickness increases (Section S2). The model-dependent sensitivity kernels means that a linearised Backus-Gilbert style inversion (Backus & Gilbert, 1970; Masters & Gubbins, 2003) cannot be applied to the problem of resolving extreme layers at the CMB.

4 Fit to Mode Dataset

For each model, the best-fitting layer thickness is assessed by calculating a least-squares misfit, M , between the observed, d , and predicted, f , centre frequencies using $N = 353$ modes. The misfit is weighted by the errors; in addition to the published ‘measurement error’, ϵ_d , we also associate a ‘model error’, ϵ_f , which is the range of eigenfrequency values from PREM, STW105 (Kustowski et al., 2008) and EPOC, representing

the variation of a mode between different 1D models. All error values used are given in Section S11.

$$M = \frac{1}{N} \sum_{i=0}^N \frac{(f_i - d_i)^2}{\epsilon_{f_i}^2 + \epsilon_{d_i}^2}. \quad (1)$$

The minimum misfit and best-fitting layer thickness are calculated for both layers (Figure 2). For many modes, the presence of a solid layer improves the fit to the measurement (Figure 2a). For the solid layer, the best-fitting layer thickness is 1.95 km, but for the molten layer is 0 km (Figures 2b-c), indicating that the modes do not prefer a molten layer and the upwards movement of the solid-fluid interface over EPOC.

We also test other background models. PREM and STW105 have best-fitting solid layer thicknesses of 2.7 km and 2.75 km, respectively (Section S4). These models differ in the upper mantle, while PREM and EPOC differ in the outer core. The different results for PREM and EPOC indicate a trade-off between structure above and below the CMB (see also Irving et al., 2018; Van Tent et al., 2020). Additionally, we show that toroidal modes independently prefer a layer (Section S5). There is also a trade-off between the strength of the seismic anomalies and the layer thicknesses (Section S6), and with lower mantle velocity structure and anisotropy (Section S7). We perform simple tests of the effects of anisotropy by including an anisotropic D'' (as in Montagner & Kennett, 1996) and anisotropy throughout the lower mantle (following De Wit & Trampert, 2015), neither of which affects the preferred layer thickness by more than 150 m. The misfit reduction cannot be achieved by moving the CMB alone (Section S8). We also test the robustness of our results by perturbing the measured and predicted centre frequencies according to the errors (Section S9); the data prefer a layer on the order of 1 km thick even accounting for underestimation in the measured uncertainties (e.g. Akbarashrafi et al., 2018).

5 Grid Search for Layer Properties

In order to further constrain the parameters, we construct a grid search over a wide parameter space, excluding a fully molten scenario. δV_p and δV_s were varied from -80% to 0% relative to PREM, while $\delta\rho$ was varied from 0% to $+80\%$. All properties were varied in intervals of 10% . We exclude models which have negative bulk modulus and all 549 remaining combinations of parameters were tested for layer thicknesses from 0 km to 20 km in 0.5 km intervals.

Figure 3 summarises the results of this search (in-depth results in Section S10). EPOC with no layer has a misfit of 1.33 and the best-fitting misfit found in the search was 0.99 (Figure 3a), an improvement of 26%. 139 models have misfits within 0.05 of this global minimum, which we term ‘well-fitting’; our initially-tested solid layer meets this criterion. The best-fitting thicknesses are concentrated at values less than 3 km indicating that the modes are generally better-fitted by thinner layers (Figure 3b). All models with extreme ($> 40\%$) values of δV_p fit poorly (Figure 3c). In contrast, there is a wide range of well-fitting values of δV_s (-10% to -80% , Figure 3d) and for density ($+10\%$ to $+80\%$, Figure 3e). It is notable that 96% of the models tested preferred the inclusion of a layer, however the wide parameter space precludes further constraint.

6 Discussion

6.1 Limitations

Our methodology does not allow us to verify that a layer must exist, but illustrates an improvement to EPOC that reduces the misfit to observations. Our results indicate

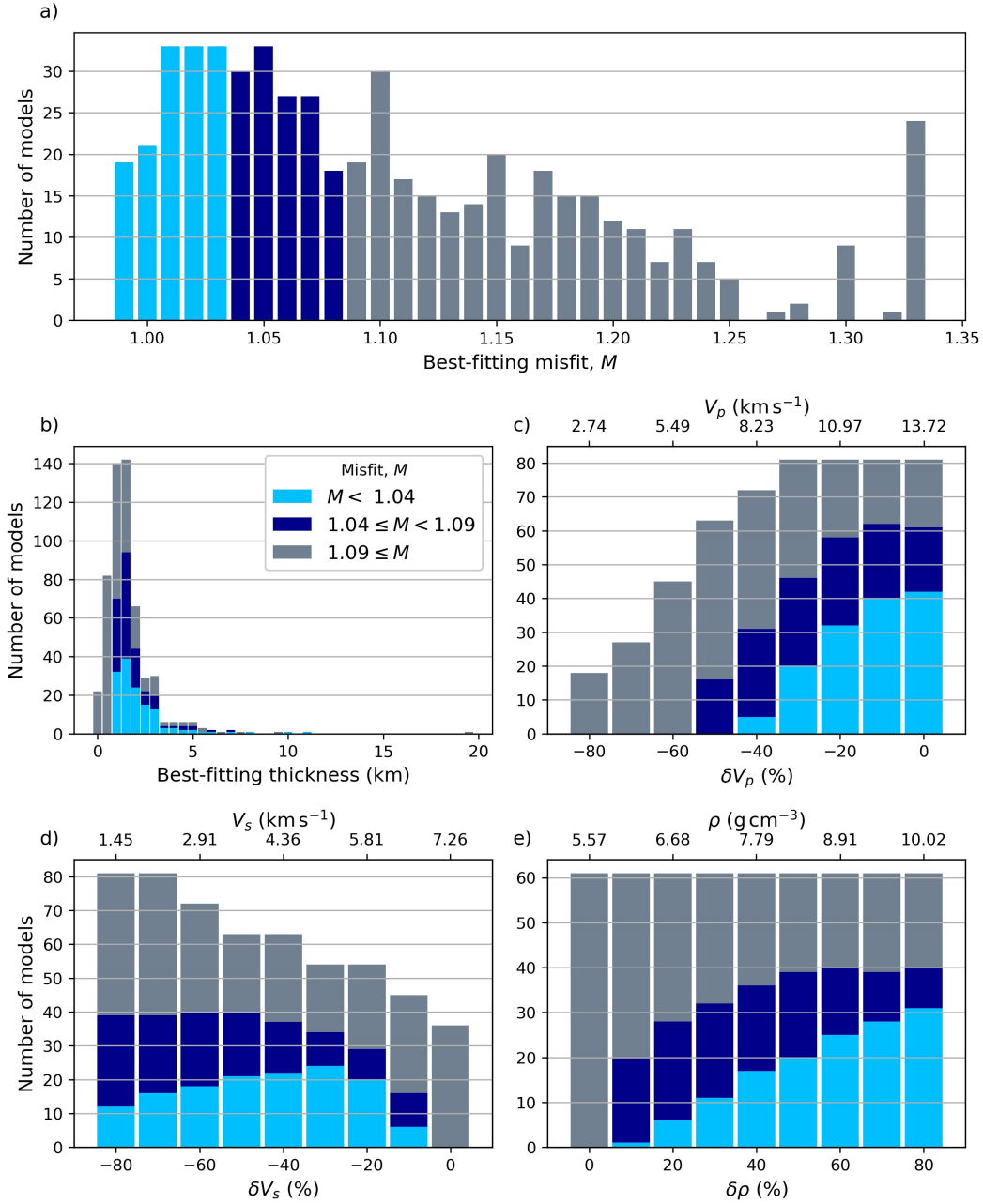


Figure 3. (a) The distribution of the best-fitting misfit values. Colours correspond to the misfit. Models in light blue ($M < 1.04$) are referred to as ‘well-fitting’. (b) Best-fitting layer thicknesses coloured by misfit. (c-e) Distribution of misfit values across the range of δV_p , δV_s and $\delta \rho$.

that a thin layer at the CMB can significantly improve the fit to normal modes. If such a structure exists, which is reasonable to suspect, then it may have not arisen in existing global 1D models due to their smooth parameterisation. Future models should therefore consider this layer in their construction. It is well known that the lowermost mantle is strongly heterogeneous and whether our results can be (partly) explained by the averaged signal of heterogeneity, such as ULVZs, and/or CMB topography requires further testing.

6.2 Comparison to Body Wave Data

PKKP_{diff} and PKKP_{bc} differential times are sensitive to the presence of thin layers atop the CMB (Russell et al., 2022). Using >12,500 observations, Russell et al. (2022) concluded a seismically anomalous layer ~1 - 2 km thick was consistent with their data, but that robust observation was inhibited by scatter. 3D structures such as ULVZs (Chen et al., 2023) and CMB topography may be a significant cause of this scatter.

Normal modes centre frequencies do not have sensitivity to these 3D structures. Furthermore, a totally molten layer in EPOC is not preferred by normal modes. This does not contradict the results of Russell et al. (2022) as PKKP_{diff} phases are only sensitive to V_p , while normal modes are also sensitive to V_s and ρ . The 1 - 2 km of -33% V_p that fits the PKKP_{diff} observations is consistent with the results of this study. Our finding that numerous models with smaller δV_s are well-fitting indicates that an examination of less extreme layers with body waves, especially CMB sensitive S-waves such as ScP, S_{diff} or SPdKS (e.g. Brown et al., 2015; Thorne et al., 2021; Li et al., 2022), may be warranted. Recent PcP observations have been used to infer the existence of a global layer of subducted material (Hansen et al., 2023) and S_{diff} observations have been found to be consistent with a slow layer underlying the entire Pacific (Wolf & Long, 2023).

Other studies have highlighted that ULVZs may be internally layered with higher proportions of melt, iron or both at their base (Thybo et al., 2003; Ross et al., 2004; Li et al., 2022). Such a layer would be seismically more anomalous and, if it was laterally more extensive than the ULVZs themselves, may be the structure that the normal modes are sensing. Ross et al. (2004) observed a ULVZ beneath Siberia and found that PcP data are fitted by a 6 km thick lower layer with -25% δV_p and -45% δV_s . These parameters agree with our constraints, and the discrepancy in thickness could be due to their observations being within a ULVZ, while ours represent a global average. Additionally Li et al. (2022) find that S_{diff} post-cursors through the Hawaiian ULVZ suggest a 2 km thick lower basal layer with -40% δV_s .

6.3 Layer Origins and Implications

A low velocity layer at the CMB may originate from melting (Q. Williams & Garnero, 1996; Dannberg et al., 2021) or iron enrichment (Wicks et al., 2010; Dobrosavljevic et al., 2019). It could be the partially-molten or solidified remnants of a basal magma ocean (Labrosse et al., 2007), the product of core-mantle chemical exchange (e.g. Stein & Hansen, 2023), buoyant core-derived solids (Mittal et al., 2020; Fu et al., 2023), or subducted material (e.g. Hansen et al., 2023). A partially molten lowermost mantle has been proposed for both the moon (Weber et al., 2011) and Mars (Samuel et al., 2021).

Figure 4 shows the occurrence of well-fitting models across the parameter space. Most well-fitting models have a $\delta V_s:\delta V_p$ ratio exceeding 1:1 and many exceed 3:1. Iron-rich ferropericase (Dobrosavljevic et al., 2019) and partial melt (Berryman, 2000; Dannberg et al., 2021) can explain these ratios. Dense partial melt in the lowermost mantle should percolate downwards, resulting in a totally molten layer atop the CMB (Hernlund & Tackley, 2007; Dannberg et al., 2021) which is not favoured by the modes. The decrease in δV_s and increase in $\delta\rho$ are relatively well-correlated in the well-fitting models which may

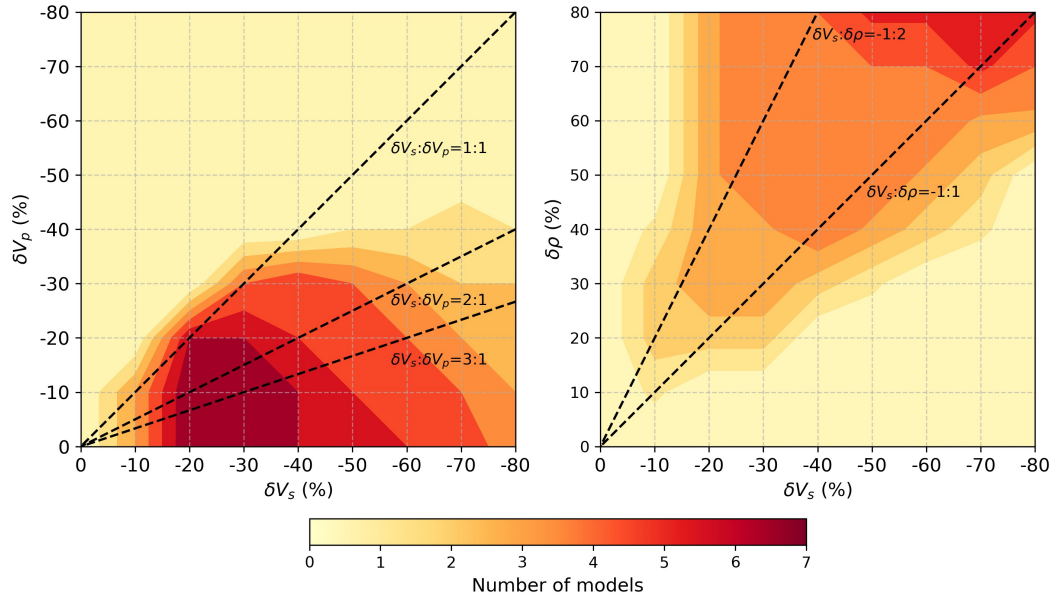


Figure 4. (a) The density of well-fitting models as a function of δV_s and δV_p . (b) as for (a) but for δV_s and $\delta \rho$. Dashed lines show anomaly ratios as labelled.

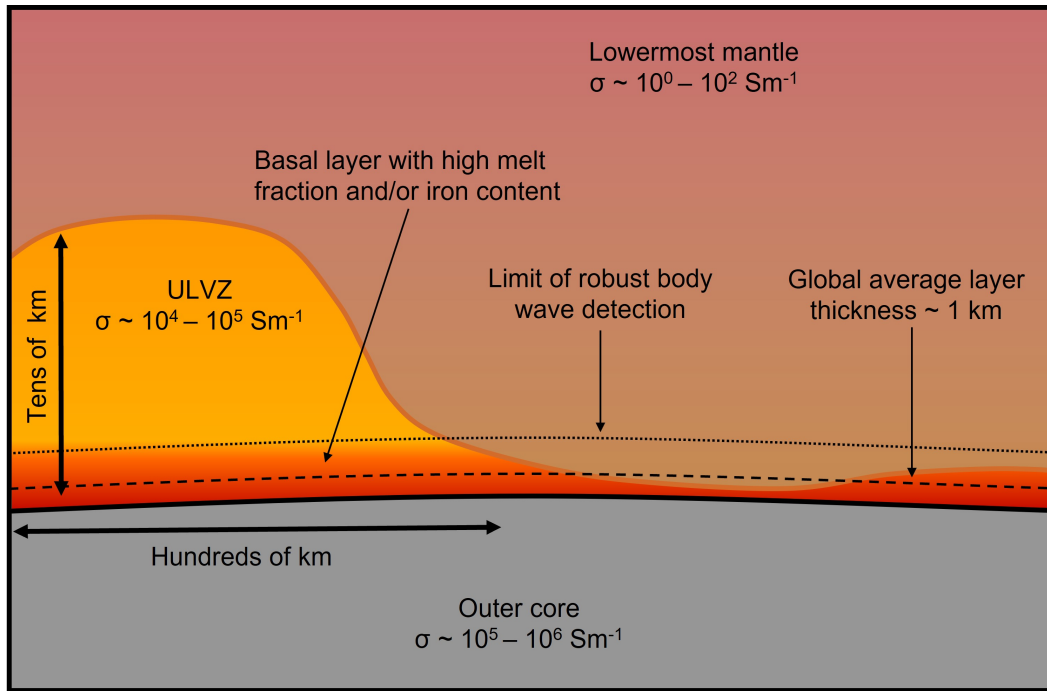


Figure 5. Cartoon demonstrating how a layer may relate to ULVZs and core-mantle interaction. σ indicates electrical conductivity.

support an iron-rich composition. Due to the wide range of well-fitting parameters we do not infer the layer’s origins, however the strongly favoured density increase may suggest a structure that is distinct from currently described ULVZs, which typically have inferred density increases up to 20% (Yu & Garnero, 2018).

Figure 5 demonstrates how a global low velocity layer may relate to ULVZs and other CMB phenomena. Constraints on lowermost mantle electrical conductivity come from observations of Earth’s length-of-day and diurnal nutations, which require electromagnetic coupling between the core and mantle with a total conductance of 10^8 S (Buffett et al., 2002; Holme, 1998). The electrical conductivity of silicates in the lowermost mantle is on the order of $10^0 - 10^2$ Sm^{-1} (Sinmyo et al., 2014), however for post-perovskite it could be greater (Ohta et al., 2008). Coupling is limited to the skin depth of magnetic diffusion, which for diurnal nutations is ~ 500 m, requiring a lowermost mantle conductivity on the order of 10^5 Sm^{-1} (Buffett et al., 2002). The conductivity of ferropericlase at CMB conditions is on the order of $10^4 - 10^5$ Sm^{-1} (Holmström et al., 2018; Ho et al., 2023), and thus iron-enrichment can satisfy both the conductance requirement and the seismology.

This layer may also provide an anomalous geochemical reservoir. Melt or iron at the CMB may enhance core-mantle interaction leading to geochemical anomalies detected at hotspots (Brandon et al., 1998; Mundl-Petermeier et al., 2020), or could itself be a primordial reservoir (C. D. Williams et al., 2015). Disentangling geochemical signatures that may relate to a layer of unknown origin would be difficult, however our results suggest that this should be considered.

7 Conclusions

We have used a dataset of 353 normal mode centre frequency measurements, coupled with a forward modelling approach, to test the visibility of a global kilometre-scale slow layer atop the CMB to normal mode centre frequencies. We find the fit of EPOC to the dataset is improved by a global slow and dense layer with an average thickness on the order of one kilometre. However, a wide range of well-fitting seismic parameters, trade-offs with layer thickness and with the choice of background model make assessment of the exact layer properties and thickness impossible.

Broadly speaking, the best-fitting models are 1 - 3 km thick, have a tens of percent (10-80%) decrease in S-velocity and increase in density, and a lesser decrease (0-40%) in P-velocity relative to PREM’s lowermost mantle. There is a preference for high $\delta V_s:\delta V_p$ ratios, which could be indicative of either partial melt or iron enrichment at the CMB. Forward modelling of normal modes cannot prove this layer is required but, when constructing future models of the Earth, it should be considered a viable structure that may improve the fit to seismic data. If a layer exists at the CMB, it would have multi-disciplinary implications for core-mantle coupling, geochemistry, and Earth’s evolution.

Acknowledgments

We thank members of the University of Cambridge Earth Science Department, specifically Carl Martin, Alex Myhill, Pallav Kant, Adam Butler, David Al-Attar and Helen Williams, as well as Tim Elliot, Simon Lock, Robert Myhill, Sebastian Rost and Rûna van Tent for insightful scientific discussions. Thanks to Vedran Lekić for providing ellipticity corrections and to Paula Koelemeijer for her question at SEDI 2022 that prompted this research. We thank the editor, Quentin Williams, and reviewers, Andrew Valentine and two anonymous, who have improved this manuscript post-submission. We acknowledge funding from the European Research Council (ERC) under the European Union’s Horizon 2020 research and innovation programme (grant agreement No. 804071-ZoomDeep).

Open Research

A table of all modes used, along with their centre frequencies and the errors employed can be found in the supplementary materials and is also available on Zenodo (Russell et al., 2023). To calculate eigenfrequencies and eigenfunctions we used MINEOS version 1.0.2 (Masters et al., 2011), published under the GPL2 license.

References

- Akbarashrafi, F., Al-Attar, D., Deuss, A., Trampert, J., & Valentine, A. (2018). Exact free oscillation spectra, splitting functions and the resolvability of Earth's density structure. *Geophysical Journal International*, *213*(1), 58–76. doi: 10.1093/gji/ggx539
- Backus, G., & Gilbert, F. (1970). Uniqueness in the inversion of inaccurate gross Earth data. *Philosophical Transactions of the Royal Society of London. Series A, Mathematical and Physical Sciences*, *266*(1173), 123–192. doi: 10.1098/rsta.1970.0005
- Berryman, J. G. (2000). Seismic velocity decrement ratios for regions of partial melt in the lower mantle. *Geophysical Research Letters*, *27*(3), 421–424. doi: 10.1029/1999GL008402
- Boukaré, C.-E., Ricard, Y., & Fiquet, G. (2015). Thermodynamics of the MgO-FeO-SiO₂ system up to 140 GPa: Application to the crystallization of Earth's magma ocean. *Journal of Geophysical Research: Solid Earth*, *120*(9), 6085–6101. doi: 10.1002/2015JB011929
- Brandon, A. D., Walker, R. J., Morgan, J. W., Norman, M. D., & Prichard, H. M. (1998). Coupled ¹⁸⁶Os and ¹⁸⁷Os evidence for core-mantle interaction. *Science*, *280*(5369), 1570–1573. doi: 10.1126/science.280.5369.1570
- Brown, S. P., Thorne, M. S., Miyagi, L., & Rost, S. (2015). A compositional origin to ultralow-velocity zones. *Geophysical Research Letters*, *42*(4), 1039–1045. doi: 10.1002/2014gl062097
- Buffett, B. A., Mathews, P. M., & Herring, T. A. (2002). Modeling of nutation and precession: Effects of electromagnetic coupling. *Journal of Geophysical Research: Solid Earth*, *107*(B4), ETG–5. doi: 10.1029/2000JB000056
- Chen, Y., Ni, S., Zhang, B., Zhao, L., Song, X., & Wang, Y. (2023). Sensitivities of diffracted PKKPab waves to the velocity structures in the lowermost mantle. *Geophysical Journal International*, *233*(3), 1617–1631. doi: 10.1093/gji/ggad033
- Coltice, N., Moreira, M., Hernlund, J., & Labrosse, S. (2011). Crystallization of a basal magma ocean recorded by helium and neon. *Earth and Planetary Science Letters*, *308*(1-2), 193–199. doi: 10.1016/j.epsl.2011.05.045
- Dahlen, F. A., & Tromp, J. (1998). *Theoretical Global Seismology*. Princeton University Press.
- Dannberg, J., Myhill, R., Gassmüller, R., & Cottaar, S. (2021). The morphology, evolution and seismic visibility of partial melt at the core-mantle boundary: Implications for ULVZs. *Geophysical Journal International*, *277*(2), 1028–1059. doi: 10.31223/X5532R
- Deuss, A., Ritsema, J., & Van Heijst, H. (2011). Splitting function measurements for Earth's longest period normal modes using recent large earthquakes. *Geophysical research letters*, *38*(4). doi: 10.1029/2010GL046115
- Deuss, A., Ritsema, J., & van Heijst, H. (2013). A new catalogue of normal-mode splitting function measurements up to 10 mHz. *Geophysical Journal International*, *193*(2), 920–937. doi: 10.1093/gji/ggt010
- De Wit, R., & Trampert, J. (2015). Robust constraints on average radial lower mantle anisotropy and consequences for composition and texture. *Earth and Planetary Science Letters*, *429*, 101–109. doi: 10.1016/j.epsl.2015.07.057

- Dobrosavljevic, V. V., Sturhahn, W., & Jackson, J. M. (2019). Evaluating the Role of Iron-Rich (Mg, Fe)O in Ultralow Velocity Zones. *Minerals*, *9*(12), 762. doi: 10.3390/min9120762
- Dziewonski, A. M., & Anderson, D. (1981). Preliminary Reference Earth Model. *Phys. Earth Planet. Inter.*, *25*(4), 297–356. doi: 10.1016/0031-9201(81)90046-7
- Dziewonski, A. M., & Gilbert, F. (1971). Solidity of the inner core of the Earth inferred from normal mode observations. *Nature*, *234*(5330), 465–466. doi: 10.1038/234465a0
- Fu, S., Chariton, S., Prakapenka, V. B., & Shim, S.-H. (2023). Core origin of seismic velocity anomalies at Earth’s core–mantle boundary. *Nature*. doi: 10.1038/s41586-023-05713-5
- Hansen, S. E., Garnero, E. J., Li, M., Shim, S.-H., & Rost, S. (2023). Globally distributed subducted materials along the Earth’s core–mantle boundary: Implications for ultralow velocity zones. *Science Advances*, *9*(14), eadd4838. doi: 10.1126/sciadv.add4838
- Hernlund, J. W., & Tackley, P. J. (2007). Some dynamical consequences of partial melting in Earth’s deep mantle. *Physics of the Earth and Planetary Interiors*, *162*(1-2), 149–163. doi: 10.1016/j.pepi.2007.04.005
- Ho, W.-G. D., Zhang, P., Haule, K., Jackson, J. M., Dobrosavljevic, V., & Dobrosavljevic, V. V. (2023). Quantum critical phase of FeO spans conditions of Earth’s lower mantle. *arXiv preprint arXiv:2301.04777*.
- Holme, R. (1998). Electromagnetic core–mantle coupling—I. Explaining decadal changes in the length of day. *Geophysical Journal International*, *132*(1), 167–180. doi: 10.1046/j.1365-246x.1998.00424.x
- Holme, R., & De Viron, O. (2013). Characterization and implications of intradecadal variations in length of day. *Nature*, *499*(7457), 202–204. doi: 10.1038/nature12282
- Holmström, E., Stixrude, L., Scipioni, R., & Foster, A. S. (2018). Electronic conductivity of solid and liquid (Mg, Fe)O computed from first principles. *Earth and Planetary Science Letters*, *490*, 11–19. doi: 10.1016/j.epsl.2018.03.009
- Irving, J. C. E., Cottaar, S., & Lekić, V. (2018). Seismically determined elastic parameters for Earth’s outer core. *Science Advances*, *4*(6), eaar2538. doi: 10.1126/sciadv.aar2538
- Irving, J. C. E., Deuss, A., & Andrews, J. (2008). Wide-band coupling of Earth’s normal modes due to anisotropic inner core structure. *Geophysical Journal International*, *174*(3), 919–929. doi: 10.1111/j.1365-246X.2008.03824.x
- Koelmeijer, P., Deuss, A., & Ritsema, J. (2013). Observations of core–mantle boundary Stoneley modes. *Geophysical Research Letters*, *40*(11), 2557–2561. doi: 10.1002/grl.50514
- Koelmeijer, P., Deuss, A., & Trampert, J. (2012). Normal mode sensitivity to Earth’s D'' layer and topography on the core–mantle boundary: what we can and cannot see. *Geophysical Journal International*, *190*(1), 553–568. doi: 10.1111/j.1365-246x.2012.05499.x
- Kustowski, B., Ekström, G., & Dziewoński, A. M. (2008). Anisotropic shear-wave velocity structure of the Earth’s mantle: A global model. *Journal of Geophysical Research: Solid Earth*, *113*(B6). doi: 10.1029/2007JB005169
- Labrosse, S., Hernlund, J. W., & Coltice, N. (2007). A crystallizing dense magma ocean at the base of the Earth’s mantle. *Nature*, *450*(7171), 866–869. doi: 10.1038/nature06355
- Li, Z., Leng, K., Jenkins, J., & Cottaar, S. (2022). Kilometer-scale structure on the core–mantle boundary near Hawaii. *Nature Communications*, *13*(1), 1–8. doi: 10.1038/s41467-022-30502-5
- Liu, J., Li, J., Hrubiak, R., & Smith, J. S. (2016). Origins of ultralow velocity zones through slab-derived metallic melt. *Proceedings of the National Academy of Sci-*

- ences, 113(20), 5547–5551. doi: 10.1073/pnas.1519540113
- Masters, G., & Gubbins, D. (2003). On the resolution of density within the Earth. *Physics of the Earth and Planetary Interiors*, 140(1-3), 159–167. doi: 10.1016/j.pepi.2003.07.008
- Masters, G., & Widmer, R. (1995). Free oscillations: frequencies and attenuations. *Global Earth Physics: a handbook of physical constants*, 1, 104.
- Masters, G., Woodhouse, J., & Freeman, G. (2011). *Mineos v1.0.2 [software]*. Retrieved from <https://geodynamics.org/resources/mineos>
- Mittal, T., Knezek, N., Arveson, S. M., McGuire, C. P., Williams, C. D., Jones, T. D., & Li, J. (2020). Precipitation of multiple light elements to power earth’s early dynamo. *Earth and Planetary Science Letters*, 532, 116030. doi: 10.1016/j.epsl.2019.116030
- Montagner, J.-P., & Kennett, B. (1996). How to reconcile body-wave and normal-mode reference Earth models. *Geophysical Journal International*, 125(1), 229–248. doi: 10.1111/j.1365-246X.1996.tb06548.x
- Mundl-Petermeier, A., Walker, R. J., Fischer, R., Lekic, V., Jackson, M. G., & Kurz, M. D. (2020). Anomalous ^{182}W in high $^3\text{He}/^4\text{He}$ ocean island basalts: Fingerprints of Earth’s core? *Geochimica et Cosmochimica Acta*, 271, 194–211. doi: 10.1016/j.gca.2019.12.020
- Ohta, K., Onoda, S., Hirose, K., Sinmyo, R., Shimizu, K., Sata, N., . . . Yasuhara, A. (2008). The electrical conductivity of post-perovskite in Earth’s D’’ layer. *Science*, 320(5872), 89–91. doi: 10.1126/science.1155148
- Reference Earth Model*. (n.d.). <https://igppweb.ucsd.edu/~gabi/rem.dir/surface/rem.surf.html>. (Accessed: 2022-11-07)
- Resovsky, J. S., & Ritzwoller, M. H. (1998). New and refined constraints on three-dimensional Earth structure from normal modes below 3 mHz. *Journal of Geophysical Research: Solid Earth*, 103(B1), 783–810. doi: 10.1029/97JB02482
- Robson, A., Lau, H. C., Koelemeijer, P., & Romanowicz, B. (2022). An analysis of core–mantle boundary Stoneley mode sensitivity and sources of uncertainty. *Geophysical Journal International*, 228(3), 1962–1974.
- Ross, A. R., Thybo, H., & Solidilov, L. N. (2004). Reflection seismic profiles of the core-mantle boundary. *Journal of Geophysical Research: Solid Earth*, 109(B8). doi: 10.1029/2003jb002515
- Rost, S., & Garnero, E. J. (2006). Detection of an ultralow velocity zone at the core-mantle boundary using diffracted PKKP_{ab} waves. *Journal of Geophysical Research*, 111(B7). doi: 10.1029/2005jb003850
- Russell, S., Irving, J. C. E., & Cottaar, S. (2022). Seismic visibility of melt at the core-mantle boundary from PKKP diffracted waves. *Earth and Planetary Science Letters*, 595, 117768. doi: 10.1016/j.epsl.2022.117768
- Russell, S., Irving, J. C. E., Jagt, L., & Cottaar, S. (2023). [database]. doi: 10.5281/zenodo.8401868
- Samuel, H., Ballmer, M. D., Padovan, S., Tosi, N., Rivoldini, A., & Plesa, A.-C. (2021). The thermo-chemical evolution of Mars with a strongly stratified mantle. *Journal of Geophysical Research: Planets*, 126(4), e2020JE006613. doi: doi.org/10.1029/2020JE006613
- Schneider, S., & Deuss, A. (2021). A new catalogue of toroidal-mode overtone splitting function measurements. *Geophysical Journal International*, 225(1), 329–341. doi: 10.1093/gji/ggaa567
- Sinmyo, R., Pesce, G., Greenberg, E., McCammon, C., & Dubrovinsky, L. (2014). Lower mantle electrical conductivity based on measurements of Al, Fe-bearing perovskite under lower mantle conditions. *Earth and Planetary Science Letters*, 393, 165–172. doi: 10.1016/j.epsl.2014.02.049
- Stein, C., & Hansen, U. (2023). Formation of Thermochemical Heterogeneities by Core-Mantle Interaction. *Journal of Geophysical Research: Solid Earth*. doi: 10

- .1029/2022jb025689
- Stoneley, R. (1924). Elastic waves at the surface of separation of two solids. *Proceedings of the Royal Society of London. Series A, Containing Papers of a Mathematical and Physical Character*, 106(738), 416–428. doi: 10.1098/rspa.1924.0079
- van Tent, R., Deuss, A., Kaneshima, S., & Thomas, C. (2020). The signal of outermost-core stratification in body-wave and normal-mode data. *Geophysical Journal International*, 223(2), 1338–1354. doi: 10.1093/gji/ggaa368
- Thorne, M. S., Leng, K., Pachhai, S., Rost, S., Wicks, J., & Nissen-Meyer, T. (2021). The most parsimonious ultralow-velocity zone distribution from highly anomalous SPdKS waveforms. *Geochemistry, Geophysics, Geosystems*, 22(1), e2020GC009467. doi: 10.1029/2020GC009467
- Thybo, H., Ross, A. R., & Egorkin, A. V. (2003). Explosion seismic reflections from the Earth’s core. *Earth and Planetary Science Letters*, 216(4), 693–702. doi: 10.1016/s0012-821x(03)00532-6
- Weber, R. C., Lin, P.-Y., Garnero, E. J., Williams, Q., & Lognonné, P. (2011). Seismic detection of the lunar core. *science*, 331(6015), 309–312. doi: 10.1126/science.1199375
- Wicks, J. K., Jackson, J. M., & Sturhahn, W. (2010). Very low sound velocities in iron-rich (Mg, Fe)O: Implications for the core-mantle boundary region. *Geophysical Research Letters*, 37(15). doi: 10.1029/2010gl043689
- Widmer-Schmidrig, R. (2002). Application of regionalized multiplet stripping to retrieval of aspherical structure constraints. *Geophysical Journal International*, 148(2), 201–213. doi: 10.1046/j.1365-246X.2002.01583.x
- Williams, C. D., Li, M., McNamara, A. K., Garnero, E. J., & Van Soest, M. C. (2015). Episodic entrainment of deep primordial mantle material into ocean island basalts. *Nature Communications*, 6(1), 1–7. doi: 10.1038/ncomms9937
- Williams, Q., & Garnero, E. J. (1996). Seismic evidence for partial melt at the base of Earth’s mantle. *Science*, 273(5281), 1528–1530. doi: 10.1126/science.273.5281.1528
- Wolf, J., & Long, M. D. (2023). Lowermost mantle structure beneath the central pacific ocean: Ultralow velocity zones and seismic anisotropy. *Geochemistry, Geophysics, Geosystems*, 24(6), e2022GC010853. doi: 10.1029/2022GC010853
- Woodhouse, J. H. (1988). The calculation of the eigenfrequencies and eigenfunctions of the free oscillations of the Earth and Sun. *Seismological algorithms: computational methods and computer programs*, 321–370.
- Woodhouse, J. H., Giardini, D., & Li, X.-D. (1986). Evidence for inner core anisotropy from free oscillations. *Geophysical Research Letters*, 13(13), 1549–1552. doi: 10.1029/GL013i013p01549
- Yu, S., & Garnero, E. J. (2018). Ultralow velocity zone locations: A global assessment. *Geochemistry, Geophysics, Geosystems*, 19(2), 396–414. doi: 10.1002/2017GC007281
- Yuan, K., & Romanowicz, B. (2017). Seismic evidence for partial melting at the root of major hot spot plumes. *Science*, 357(6349), 393–397. doi: 10.1126/science.285.5433.1545
- Zou, Z., Leyton, F., & Koper, K. D. (2007). Partial melt in the lowermost mantle near the base of a plume. *Geophysical Journal International*, 168(2), 809–817. doi: 10.1111/j.1365-246X.2006.03266.x

Supplementary Materials for: **Evidence for a kilometre-scale seismically slow layer atop the core-mantle boundary from normal modes**

Stuart Russell^{1,2}, Jessica C.E. Irving³, Lisanne Jagt¹, Sanne Cottaar¹

¹ University of Cambridge, United Kingdom

² Universität Münster, Germany

³ University of Bristol, United Kingdom

This document includes:

1. A selection of sensitivity kernels for normal modes in different velocity models.
2. A demonstration of the different behaviour of eigenfrequencies for the solid and molten layers.
3. An extended results section containing eigenfrequency and measured value comparison for all modes.
4. A comparison of the results when the background model is changed from EPOC to PREM or STW105.
5. A comparison of the results for toroidal and spheroidal modes separately.
6. An exploration of the trade-offs between the strength of the seismic parameters and thickness.
7. An exploration of the trade-offs with wider D'' structure and lower mantle radial anisotropy.
8. An exploration of the effect of changing the CMB radius.
9. A discussion of the treatment of errors and an exploration of the robustness of the results.
10. Further presentation of results from the grid search.
11. Further details on the construction of the mode dataset, and a table of the included modes.

1 The impact of the model on sensitivity kernels

Sensitivity kernels provide a description of the sensitivity of the centre frequency of a particular mode to different parameters at depths within a model. Kernels are calculated from the eigenfunctions outputted from MINEOS (*Masters et al.*, 2011) using the formulation from *Dahlen and Tromp* (1998). The eigenfunctions, and therefore the sensitivity kernels, depend on the model that the mode is oscillating within. In this section we demonstrate how the behaviour of selected modes changes between different models.

Figures S1-S5 show how the kernels change for five selected modes in both PREM (*Dziewonski and Anderson*, 1981) and EPOC (*Irving et al.*, 2018) with and without layers. Some modes, such as ${}_2S_{16}$ (Figure S1) change minimally between different models even when a layer is included. Others drastically change their behaviour, for example ${}_3S_{26}$ (Figure S2) which ceases to be a Stoneley mode (*Stoneley*, 1924; *Koelemeijer et al.*, 2013) when a layer is included in EPOC, and ${}_3S_{41}$ (Figure S3) which becomes a Stoneley mode in both PREM and EPOC when a layer is included. Even for some modes which do not change significantly throughout most of the Earth, the sensitivity at the CMB is enhanced when a layer is included. This can be clearly seen for ${}_{15}S_{15}$ (Figure S3) where the S-velocity and density sensitivities are strongly enhanced inside the layer. Layers with more extreme parameters also cause more prominent peaks in the kernels within the layer, as can be seen by comparing panels (d) and (e). ${}_3T_{16}$ (Figure S5) as a toroidal mode has no sensitivity to the outer core, hence does not change between PREM and EPOC, but does have enhanced density sensitivity within the layer. This behaviour of enhanced density sensitivity but not S-velocity is a prevalent feature of the toroidal modes in the dataset.

While the kernels do evolve as layer thickness is increased, drastic changes to the kernels (for example for ${}_3S_{26}$ and ${}_3S_{41}$ in Figures S2 and S3) are the result of ‘mode swapping’, where, due to mode naming conventions, the definition of the mode changes as the model is perturbed greatly. For ${}_3S_{26}$ and ${}_3S_{41}$ the modes swap with ${}_2S_{26}$ and ${}_3S_{41}$ respectively. Eigenfunctions are assigned to mode names based on assumptions about the Earth and it is not possible to know for certain the ‘correct’ mode to use. In the methodology presented in the main paper, modes for which this is problematic are generally suppressed by having a high model error and do not strongly influence the results. Nevertheless, this demonstrates that the behaviour of some commonly used modes is complex when the model is perturbed very strongly, resulting in difficulties in interpretation.

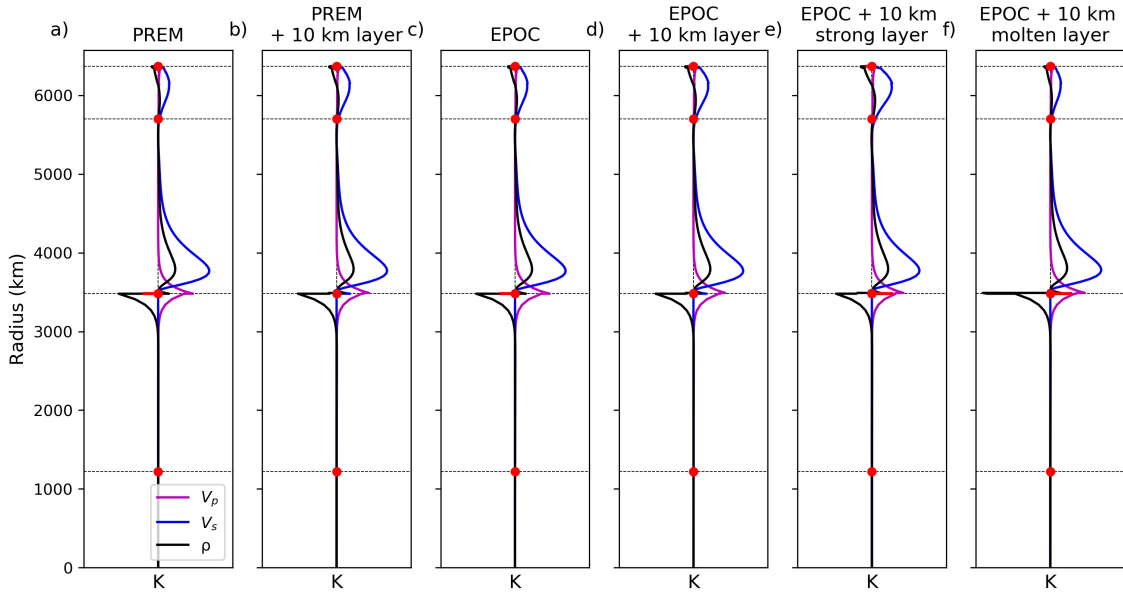


Figure S1: Sensitivity kernels for P-velocity (magenta), S-velocity (blue), density (black) and the displacement of major discontinuities (red) as a function of radius for mode ${}_2S_{16}$ in (a) PREM, (b) PREM with a 10 km thick solid layer, (c) EPOC, (d) EPOC with a 10 km thick solid layer ($\delta V_p: -20\%$, $\delta V_s: -40\%$ and $\delta \rho: +50\%$) and (e) EPOC with a 10 km thick solid layer where the parameters are twice as extreme, and (f) EPOC with a 10 km thick molten layer ($\delta V_p: -33\%$, $\delta V_s: -100\%$ and $\delta \rho: +14\%$). Horizontal dashed lines represent the major discontinuities: the surface, 660 km, core-mantle boundary (CMB) and inner-core boundary (ICB). Maximum amplitudes are consistent between subplots.

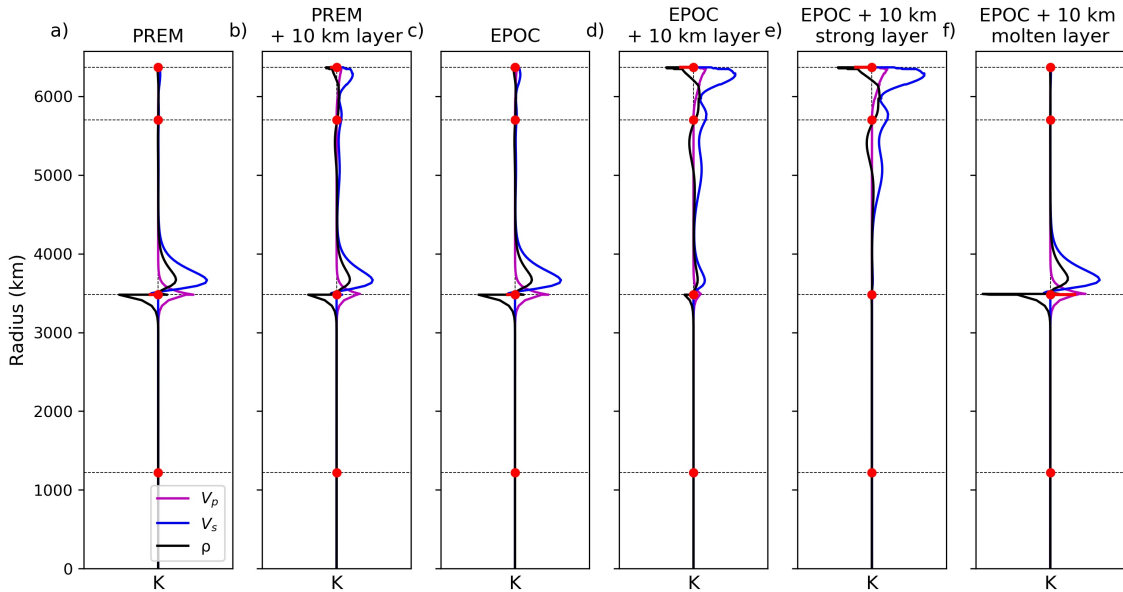


Figure S2: As Figure S1, for mode ${}_3S_{26}$.

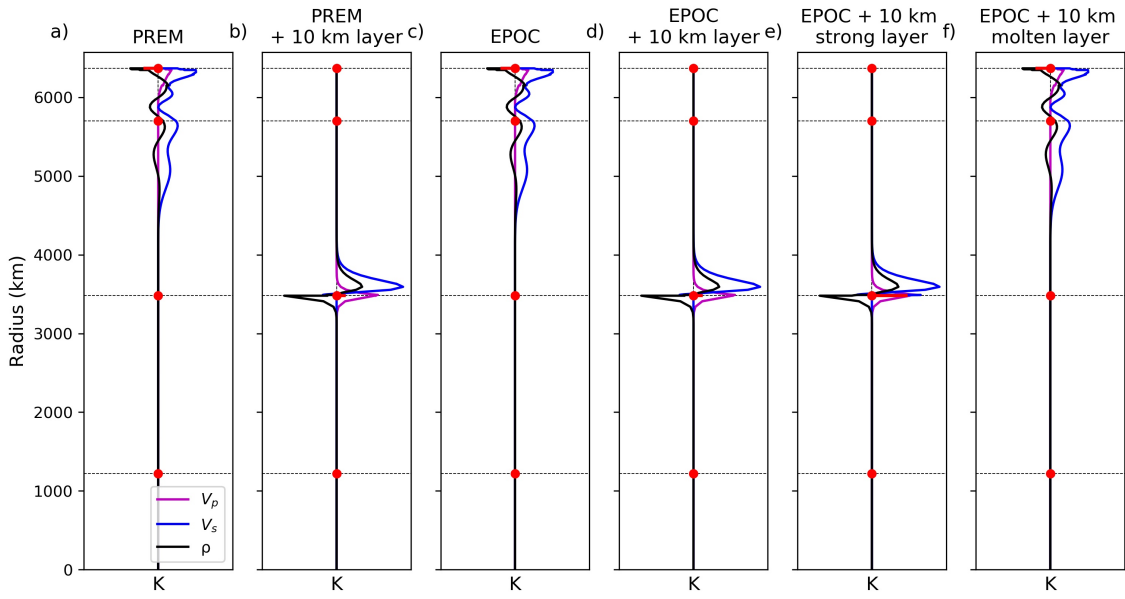


Figure S3: As Figure S1, for mode ${}_3S_{41}$.

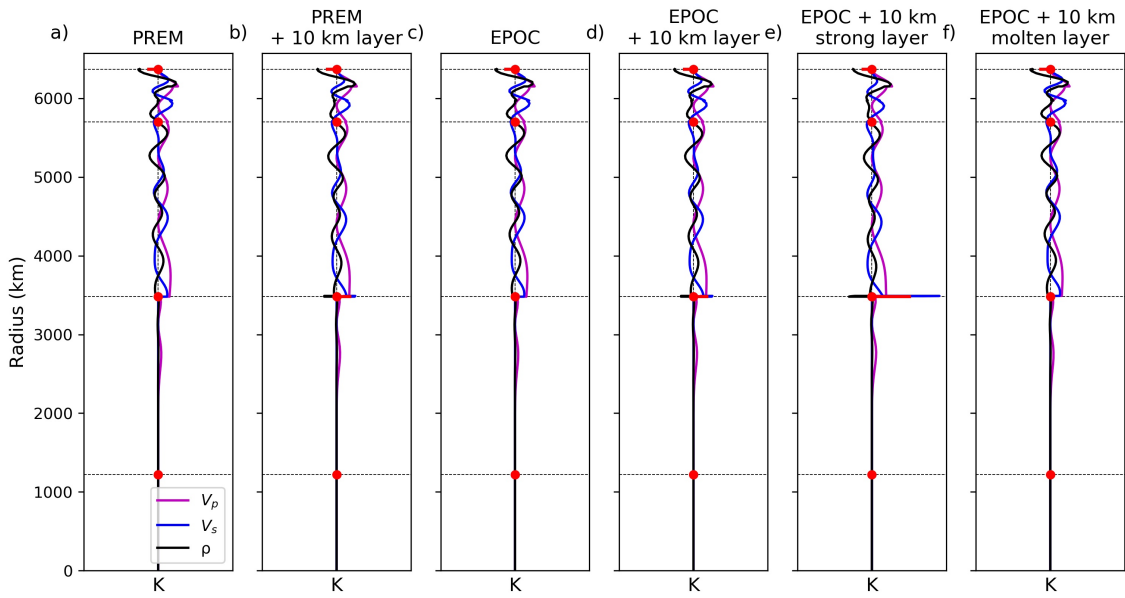


Figure S4: As Figure S1, for mode ${}_{15}S_{15}$.

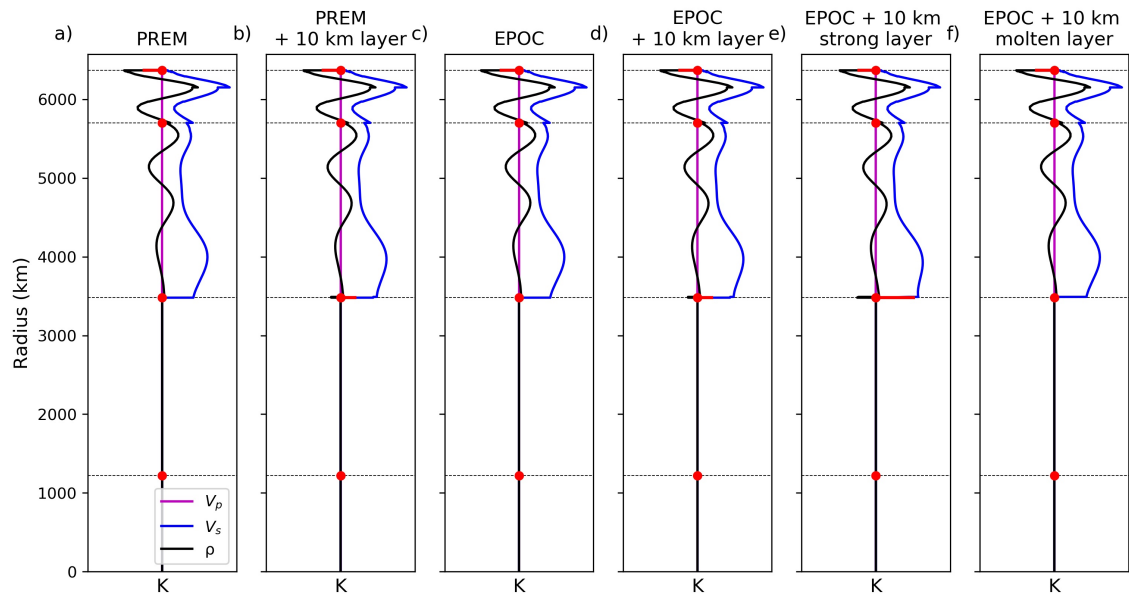


Figure S5: As Figure S1, for mode $3T_{16}$.

2 Behaviour of individual modes

Figure S6 shows the eigenfrequencies predicted by MINEOS, of four selected modes as a function of increasing layer thickness for both the solid and molten layers. For all modes, the effect of the solid layer is to decrease the eigenfrequency, however the effect of the molten layer varies between modes. The sensitivity of a mode can be approximated by the rate of change of the eigenfrequency with layer thickness; this is the gradient of a given line in Figure S6. Some modes such as ${}_1T_{14}$ (Figure S6a) behave very similarly for both the solid and molten layer, others such as ${}_0S_3$ (Figure S6b) show similar behaviour but different sensitivities. A number of modes, including ${}_{15}S_{15}$ (Figure S6c), are particularly sensitive only to one layer type. Other modes show vastly different behaviours for the different layers as can be seen for ${}_3S_{26}$ (Figure S6d). This behaviour of the solid layer decreasing the eigenfrequency while the molten layer increases it is prevalent amongst the modes of the dataset, with 245 out of 353 modes showing this behaviour.

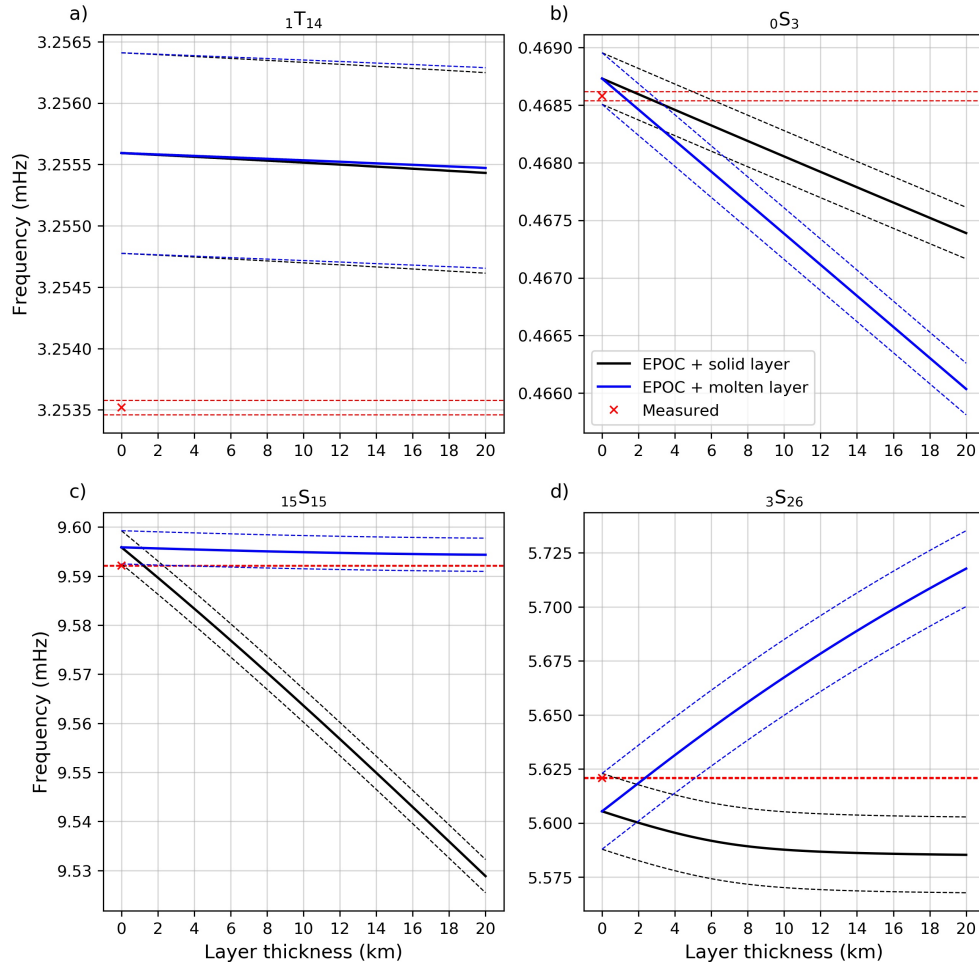


Figure S6: Centre frequency, as a function of layer thickness for four modes: (a) ${}_1T_{14}$, (b) ${}_0S_3$, (c) ${}_{15}S_{15}$ and (d) ${}_3S_{26}$. Solid lines are for the solid layer (black, $\delta V_p: -20\%$, $\delta V_s: -40\%$ and $\delta \rho: +50\%$) and molten layer (blue, $\delta V_p: -33\%$, $\delta V_s: -100\%$ and $\delta \rho: +14\%$) with dashed lines showing the model error, ϵ_f . The measured centre frequency is plotted as a red cross and the red dashed lines show the measurement error, ϵ_d .

3 Results for all modes

Figures S7 and S7 show the change in eigenfrequency for different modes relative to the measured centre frequencies. This is equivalent to Figure 4(a) in the main paper but for all 353 modes used. These modes are also sorted by gradient with the most sensitive first (gradients are given in Table S1 in Section S8). It can be seen that the width of coloured band is thickest for the most sensitive modes as is expected.

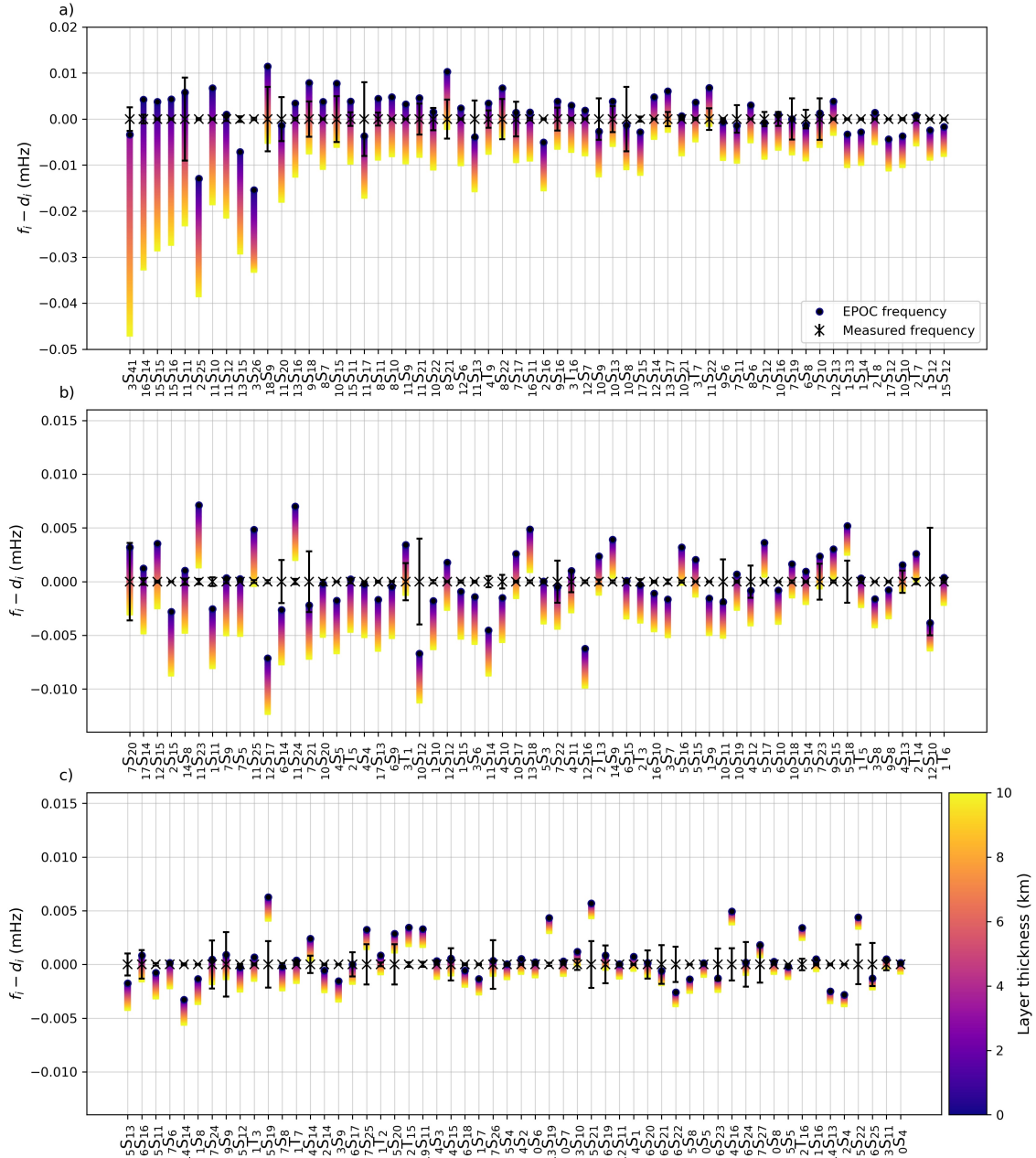


Figure S7: Colours showing the change in eigenfrequencies predicted for different thicknesses of the solid layer in EPOC, f_i , relative to the measured centre frequencies, d_i , (black cross) for different layer thicknesses. These plots show the 177 most sensitive modes ordered by gradient with the most sensitive modes to the top left. Note that (a) has a different y-axis scale.

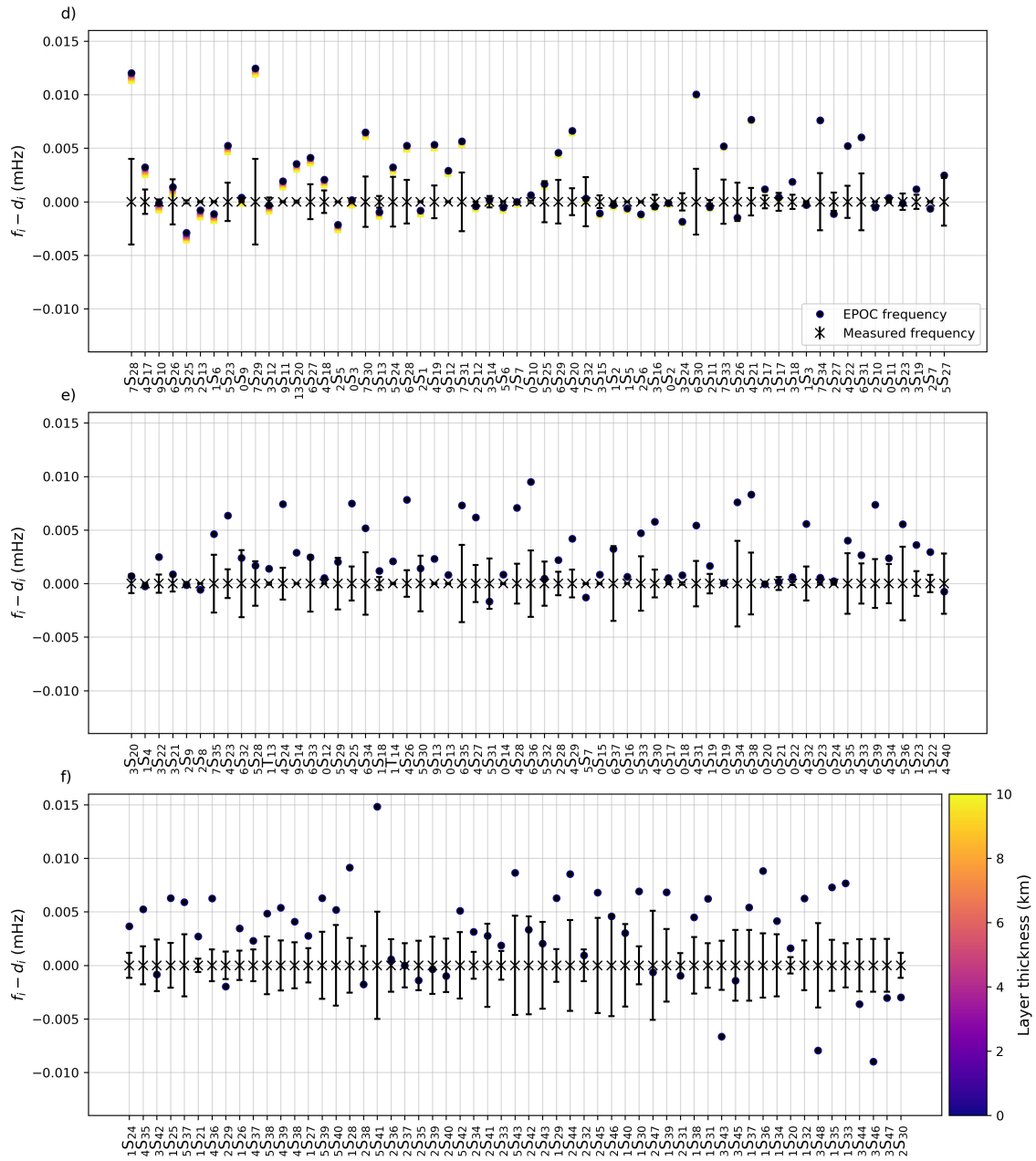


Figure S7: (Continued) Colours showing the change in eigenfrequencies predicted for different thicknesses of the solid layer in EPOC, f_i , relative to the measured centre frequencies, d_i , (black cross) for different layer thicknesses. These plots show the 176 least sensitive modes ordered by gradient with the most sensitive modes to the top left. The scales on the y-axes are consistent with panels (b) and (c).

4 The effect of the choice of background model

Figure S8 shows results in the same format as Figure 4 of the main paper but for when PREM is used as the background model as opposed to EPOC. We also test STW105 (*Kustowski et al.*, 2008) as a background model. PREM and EPOC differ in the outer core, while PREM and STW105 differ in the upper mantle. It should be noted that the most sensitive n modes are not the same for PREM, STW105 and EPOC due to differences in mode sensitivity for the different models, hence why the modes appearing in panel (a) differ between models.

For PREM and STW105 the best-fitting layer thickness is 2.7 km and 2.75 km, respectively, which is substantially thicker than the preferred thickness of 1.9 km for EPOC. That there is a difference between these two models and EPOC indicates that there is trade-off between structures above and below the CMB. The differences in the outer core in EPOC, notably a lower velocity immediately below the CMB, can account for some of the misfit between PREM, STW105, and the observed centre frequencies. That the PREM and STW105 solutions are very similar indicates that there is little trade-off with upper mantle structure.

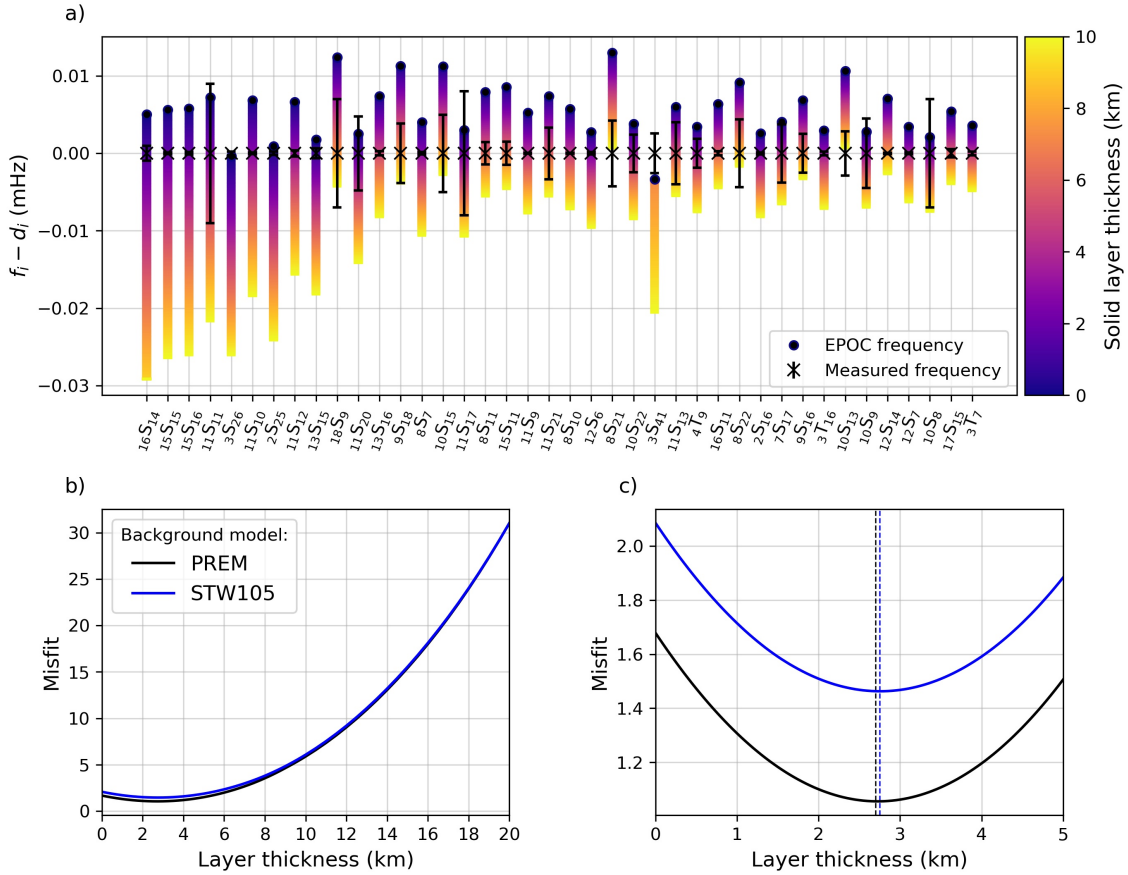


Figure S8: As Figure 2 in the main paper but testing the effect of the background model. (a) Colours showing the change in eigenfrequencies predicted for different thicknesses of the solid layer in PREM, f_i , relative to the measured centre frequencies, d_i , (black cross) for different layer thicknesses. Measurement errors, ϵ_d , are the black error bars. These are the 40 most sensitive modes ordered by their sensitivity to the inclusion of a layer. (b) and (c) show the misfit, M , as a function of layer thickness between 0 - 20 km and 0 - 5 km, respectively, for solid layers in PREM (black) and STW105 (blue). The vertical dotted line marks the minima in M .

5 A comparison of toroidal and spheroidal mode results

Toroidal and spheroidal modes are very different in their behaviour and sensitivities - spheroidal modes have radial and tangential motion analogous to P-SV motion, while toroidal modes are purely tangential and are analogous to SH motion. Toroidal modes therefore have no sensitivity to P-velocity and also have no displacement or sensitivity in fluid parts of the Earth. When studying the CMB this is notable as toroidal mode energy must be zero below the CMB.

Toroidal mode measurements are difficult to make and in the last two decades only one dataset of toroidal mode measurements has been published (*Schneider and Deuss, 2021*); our dataset contains the 19 modes from *Schneider and Deuss (2021)*. Toroidal modes are sensitive to the inclusion of a solid CMB layer and there are three toroidal mode in the 50 most sensitive modes, and a total of nine in the 100 most sensitive modes.

Figure S9a shows the results for individual toroidal modes, many of which favour non-zero layer thickness. Figures S9b-c show the results for toroidal and spheroidal modes separately. For toroidal modes there is no difference in the results between PREM and EPOC owing to the fact that toroidal modes have no outer core sensitivity. The toroidal modes have a preferred layer thickness of 2.35 km, thicker than the spheroidal preference of 1.8 km. The reason for this difference is unclear but may be related to unmodelled lower mantle anisotropy as the PREM (and therefore EPOC) lower mantle is isotropic, as is the layer we include. Alternatively this discrepancy could result from sensitivity to different parameters - toroidal modes are more sensitive to density at the CMB and have no sensitivity to P-velocity.

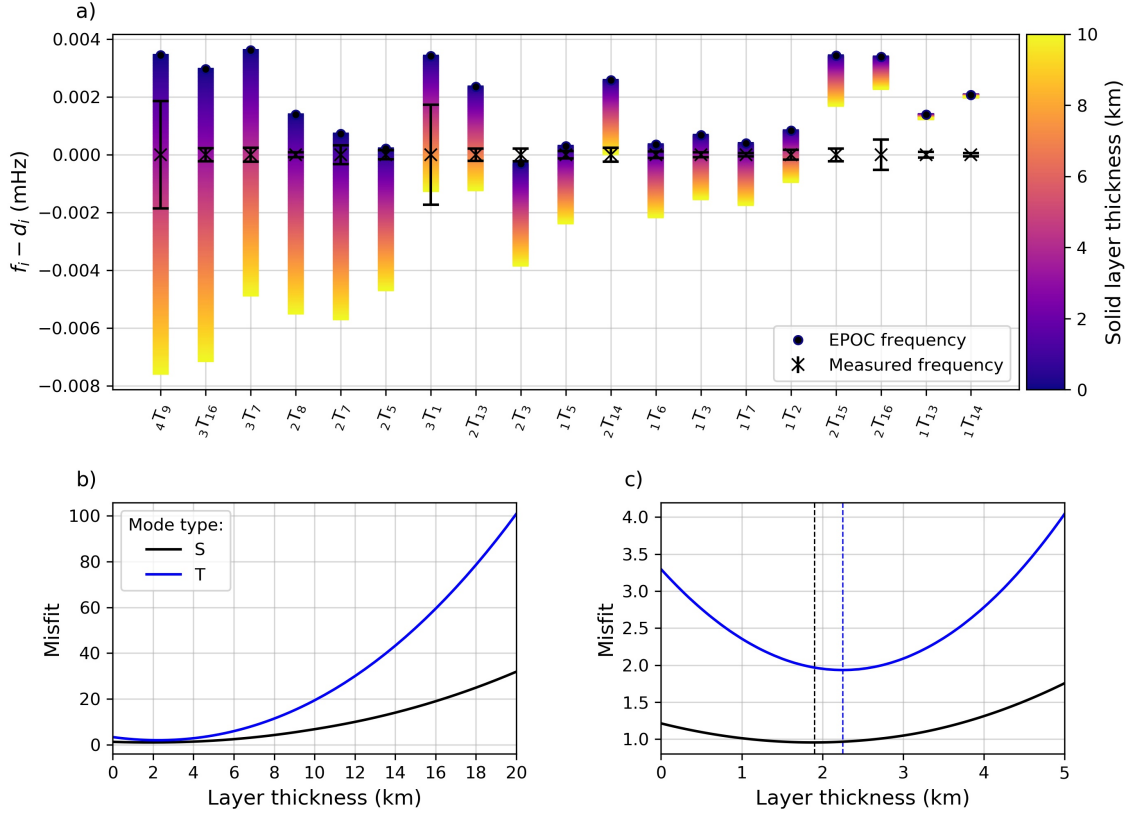


Figure S9: As Figure 2 in the main paper but highlighting the behaviour of toroidal modes. (a) Colours showing the change in eigenfrequencies predicted for different thicknesses of the solid layer in EPOC, f_i , relative to the measured centre frequencies, d_i , (black cross) for different layer thicknesses. Measurement errors, ϵ_d , are the black error bars. These are the 40 most sensitive modes ordered by their sensitivity to the inclusion of a layer. (b) and (c) show the misfit, M , as a function of solid layer thickness between 0 - 20 km and 0 - 5 km, respectively, for spheroidal (black) and toroidal (blue). The vertical dotted line marks the minima in M .

6 Trade-off with thickness and layer strength

Layer parameters were also varied in severity from those of the solid layer in the main paper. Figure S10 shows the trade-off between the strength of the seismic parameters of a layer and its best-fitting thickness, as well as the misfit at this best-fitting value for the solid layer. Less extreme layers are better fitting when they are thicker; this is expected but represents a significant source of non-uniqueness in the solution, especially as the misfit does not change significantly across the range of strengths tested. Thicker and less extreme layers are marginally better fitting but this is insignificant compared to the effect of including a velocity reduction at all.

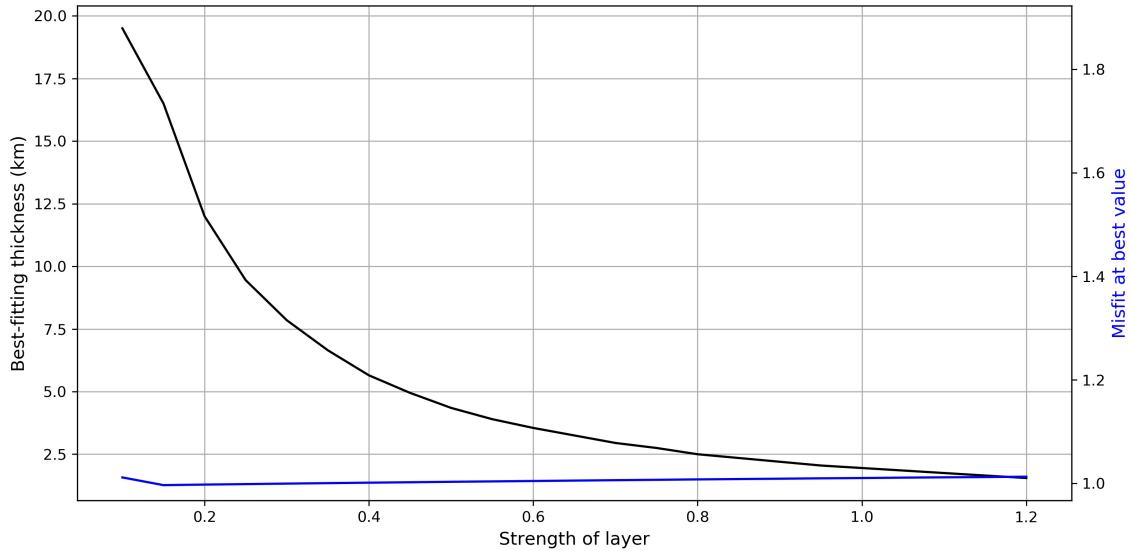


Figure S10: Best-fitting layer thickness (black) and the misfit at this value (blue) as a function of the strength of the layer. Strength is defined such that a strength of 0 is PREM parameters while a strength of 1 are the solid layer parameters given in the main paper. Therefore strength values between 0 and 1 are linearly intermediate between PREM and the layer, while strengths greater than 1 have parameters more extreme than the original layer. The y-axis for the misfit is scaled the same as Figure 4c in the main paper.

7 Trade-offs with D'' structure and lower mantle anisotropy

We also test the effect of varying structure in the wider lowermost mantle to examine how this trades-off with the preferred layer thickness. First we perform a simple test with wider D'' structure by decreasing the S-velocity of D'' uniformly from 2741 km to 2891 km in EPOC and recalculate how the misfit varies with layer thickness for this background model. We also perform the same test for increased density. We include these tests simply to highlight the trade-offs in our results, motivated by studies that have suggested that D'' may be dense or have reduced S-velocity relative to PREM (e.g. *Montagner and Kennett, 1996; De Wit and Trampert, 2015*). The results are shown in Figure S11.

It is apparent that trade-offs with wider D'' structure do exist, however in all cases tested the best-fitting results were still a layer of the same order of magnitude thickness. The results for the V_s reduction are especially interesting as without considering a thin layer, a reduced V_s throughout D'' is better-fitting than PREM, yet when a thin layer is allowed the best-fitting solution is to concentrate the velocity reduction into this layer. These tests are not comprehensive and the results should not be over-interpreted, however they do highlight the trade-offs that exist between thin and D''-wide properties in the lowermost-mantle.

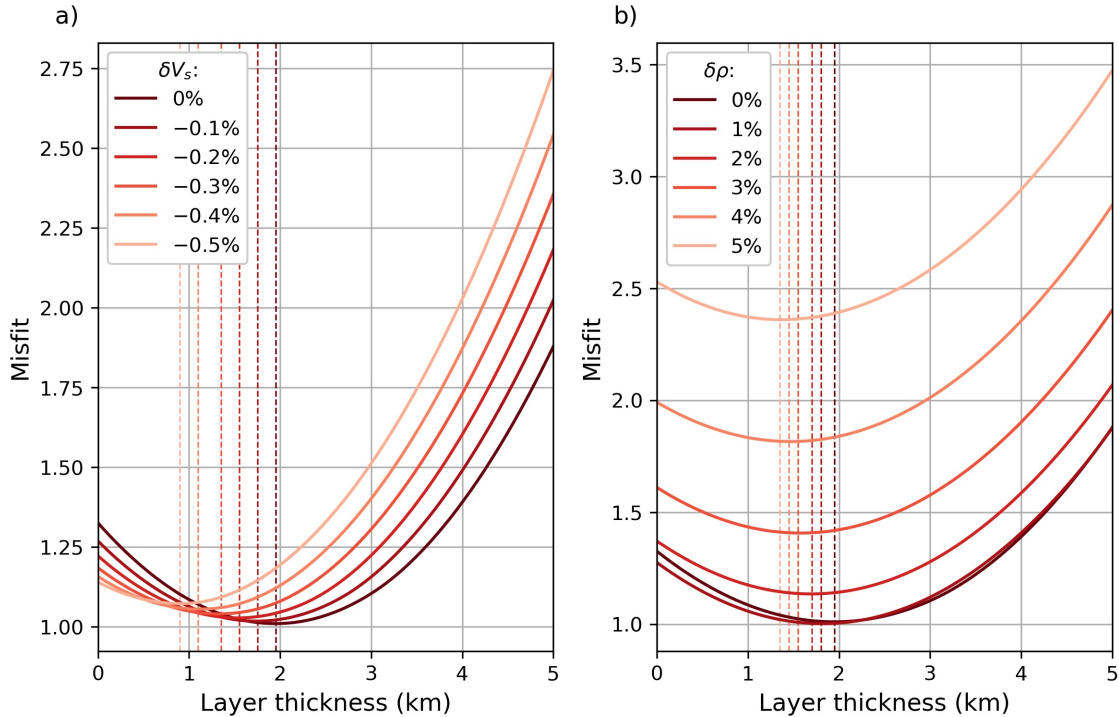


Figure S11: Misfit curves as a function of layer thickness as the background structure of D'' is varied uniformly for (a) S-velocity and (b) density. Dashed vertical lines mark the best fitting layer thicknesses.

We also perform simplistic tests with lower mantle radial anisotropy. It is well known that parts of the upper mantle are radially anisotropic (e.g. see *Dziewonski and Anderson, 1981*), and there are now several studies that suggest lower mantle radial anisotropy based on normal mode observations (e.g. *Montagner and Kennett, 1996*; *De Wit and Trampert, 2015*). We perform two tests, one with a radially anisotropic D'' and one with radial anisotropy present throughout the lower mantle. These tests are again overly simplistic and should not be over-interpreted as they are only performed to assess whether anisotropy has a significant affect on our results.

We first test the effect of an anisotropic D'' with anisotropy in the ϕ and η parameters (as per the ak135f line from Figure 12 of *Montagner and Kennett, 1996*). A more recent study has found similar anisotropic parameters for D'' , albeit with great posterior uncertainty (*De Wit and Trampert, 2015*). The aim of this test is not to assess the viability of these models, but simply to assess whether possible D'' impacts our results. We therefore include uniform anisotropy of $\phi = 1.04$ and $\eta = 1.02$ throughout D'' , keeping the background model as EPOC. We calculate the best-fitting layer thickness, which for this model is 1.85 km, 100 m less than for isotropic EPOC.

We also test radial anisotropy throughout the lower mantle in the ϕ and η parameters (*De Wit and Trampert, 2015*). Following Figure 1 of *De Wit and Trampert (2015)*, we weakly reduce ϕ through the lower mantle and we reduce η weakly in the depth range 1450 - 1900 km and more strongly below 1900 km. In order to test lower mantle anisotropy independently to D'' , and given the large posterior uncertainties in D'' anisotropy, we keep D'' isotropic. We again calculate the best-fitting layer thickness, which is 1.8 km, 150 m less than for isotropic EPOC.

Both of the tests described above indicate that anisotropy in the lower mantle does affect our results, but not significantly enough to undermine the conclusions presented in the main paper.

8 The effect of altering the radius of the CMB

Given that the misfit is lowest with a velocity reduction above the CMB, we also test whether the same result can be achieved by altering the CMB radius. In PREM and EPOC the CMB radius is 3480 km and we vary it between 3475 km and 3485 km by compressing or expanding the outer core or lower mantle up to 660 km. The results are shown in Figure S12. The best-fitting CMB radius is 3479.55 km, closer to the value of ak135 (*Kennett et al., 1995*) than of PREM, however the misfit is not as low as introducing a low velocity layer indicating that altering the CMB radius alone cannot explain our results. It is possible that there are trade-offs between CMB radius, upper outer core structure, and any slow layering atop the CMB, however a full exploration of this is beyond the scope of this study.

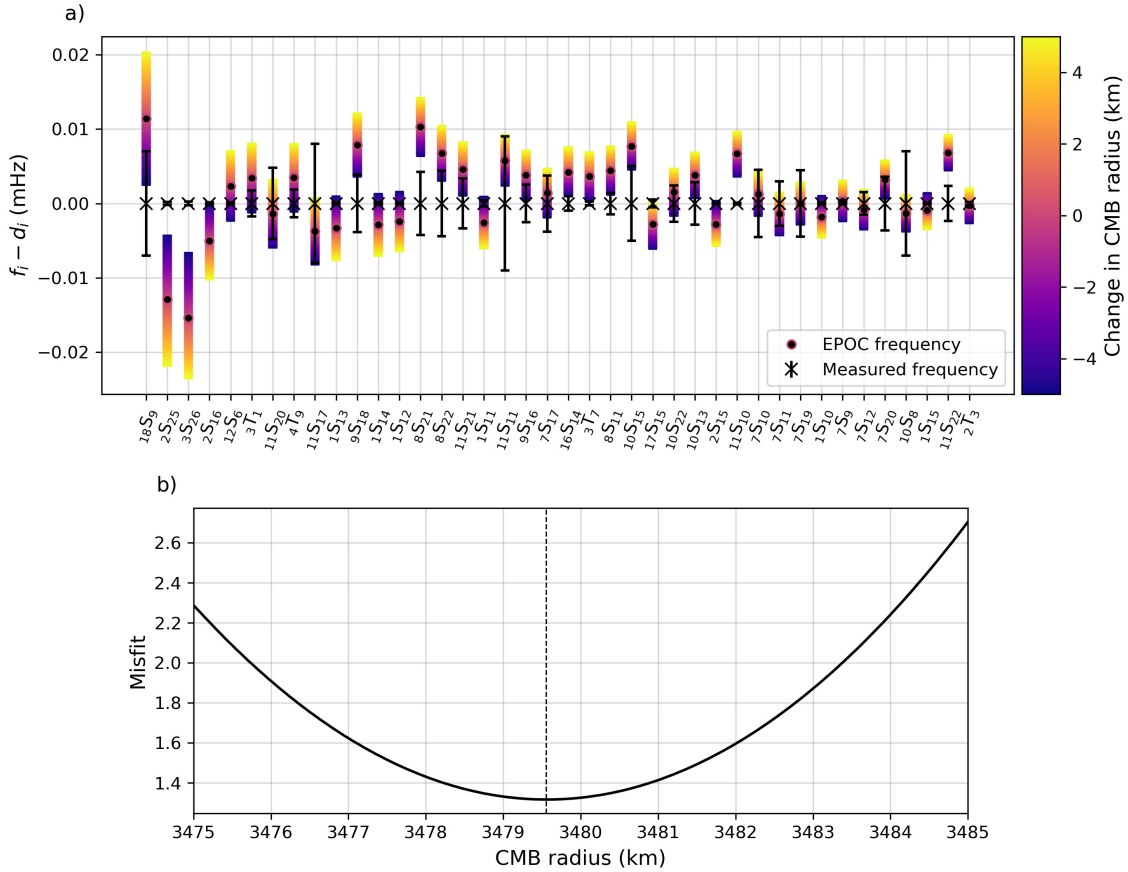


Figure S12: Similar to Figure 2 in the main paper but for models with testing the effect of changing CMB radii. (a) Colours showing the change in eigenfrequencies predicted for different CMB radii in EPOC, f_i , relative to the measured centre frequencies, d_i , (black cross) for different layer thicknesses. Measurement errors, ϵ_d , are the black error bars. These are the 40 most sensitive modes ordered by their sensitivity to moving the CMB. (b) misfit, M , plotted as a function of CMB radius. The vertical dotted line marks the minimum in M .

9 Treatment of Errors

Akbarashrafi et al. (2018) have shown that published uncertainties of splitting function measurements, and by extension of centre frequencies, are likely significantly underestimated. This is especially true for uncertainties estimated by cross-validation which do not account for errors originating outside of the measurement process, such as theoretical approximations, which may introduce systematic errors.

In the dataset used for this study, uncertainties from publications that estimate their uncertainties by cross-validation (*Deuss et al.*, 2013; *Koelemeijer et al.*, 2013; *Schneider and Deuss*, 2021) are especially small, and for the purpose of this section will be referred to as DKS modes. Within the dataset, the mean measurement error on DKS modes is a factor of 15.875 times smaller than from other sources. This is primarily because these uncertainties are defined differently, however these measurements are also more recent and are made with more, and better quality, data. Furthermore in the dataset, the DKS modes are primarily lower l (all modes where $l < 9$ are DKS modes), with smaller magnitude centre frequencies which are typically better constrained (the mean centre frequency of DKS modes is 4.56 mHz in contrast to 6.80 mHz for other modes). It is therefore not true that the uncertainties are underestimated by a factor of 15.875, but rather by an unknown smaller value. We chose not to increase the measurement errors by an arbitrary amount and instead use the published values regardless. We investigate the validity of this below.

Firstly we test how the best-fitting layer thickness for the solid layer changes when different combinations of errors are used. We do this by changing the denominator of the misfit equation in the main paper. The results are shown in Figure S13. We test the equation with no weighting by errors (denominator equal to 1), weighting by only the measurement error and weighting by a combination of both measurement and model error. For the final two scenarios, we also test with the measurement errors on DKS modes multiplied by 15.875, which is then an over-estimation of the uncertainty. In all cases, the best-fitting thickness is non-zero and the underestimated uncertainties do not change the results significantly enough to change the conclusions or interpretations.

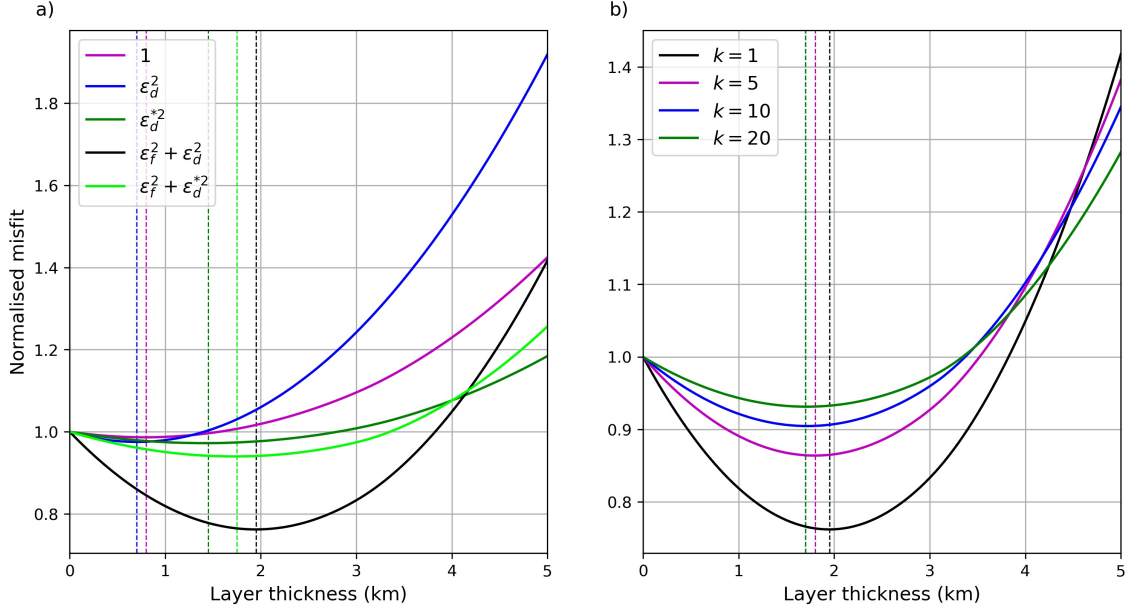


Figure S13: The misfit as a function of layer thickness when different error combinations are used. Each line uses a different denominator for the misfit equation as given in the legend and is normalised to the EPOC misfit. ϵ_d^* indicates that the measurement errors on DKS modes only are increased by a factor of 15.875. In (b), the denominator used in the misfit equation is $\epsilon_f^2 + (k\epsilon_d)^2$.

Even if the underestimated uncertainties do not change the results, they will affect the robustness of them. In order to see how these propagate through our method we perturb both the measured and modelled centre frequencies randomly based on a Gaussian with standard deviation equal to the measurement and model errors, respectively. A demonstration of this is given in Figure S14. We also repeat this where the measurement errors on DKS modes are multiplied by 15.875, and where all measurement errors are increased uniformly. For each scenario we perform 1,000,000 iterations and assess the spread in the resulting best-fitting thicknesses of the solid layer.

The results of this analysis are shown in Figure S15. With the original measurement errors, the best-fitting thickness varies considerably, but is always thicker than 1 km. When the measurement errors on DKS modes are increased, the best-fitting thickness varies more, as would be expected, but remains non-zero in all but 3 out of one million iterations. When all measurement errors are increased by a factor of 10, only one in one million iterations preferred no layer. When they are increased by a factor of 20, 0.03% of iterations preferred no layer. We must therefore conclude that the modes robustly favour the presence of a layer regardless of any underestimation of the uncertainties.

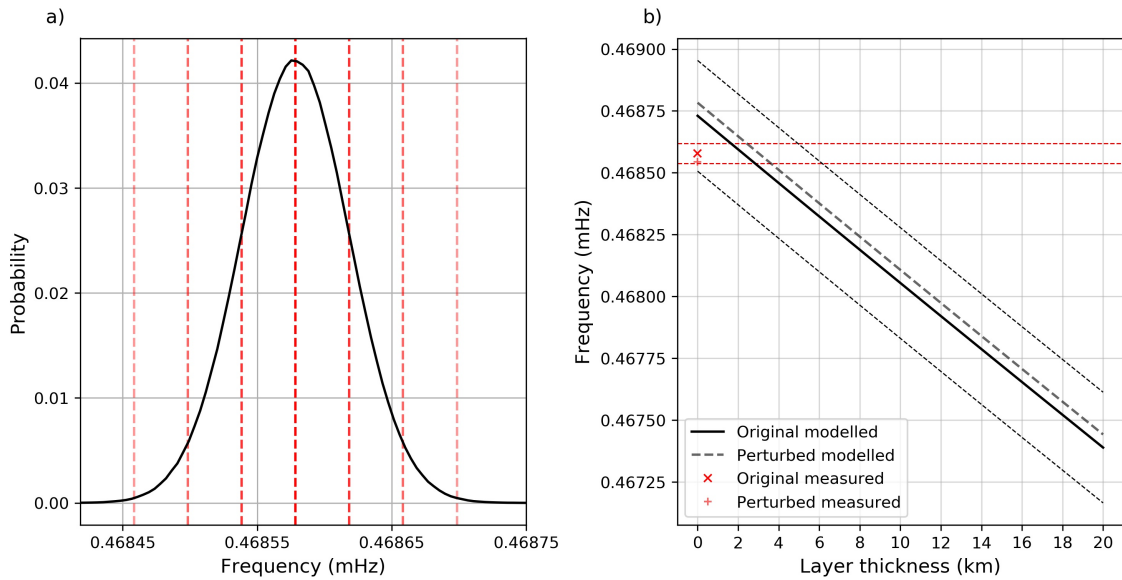


Figure S14: Demonstration of how the measured and modelled centre frequencies are perturbed for mode ${}_0S_3$. (a) a Gaussian distribution centred on the centre frequency of ${}_0S_3$ with standard deviation equal to the measurement error. Vertical red dashed lines mark 0, 1, 2, and 3 standard deviations. (b) an example demonstrating how the measured and modelled centre frequencies are perturbed.

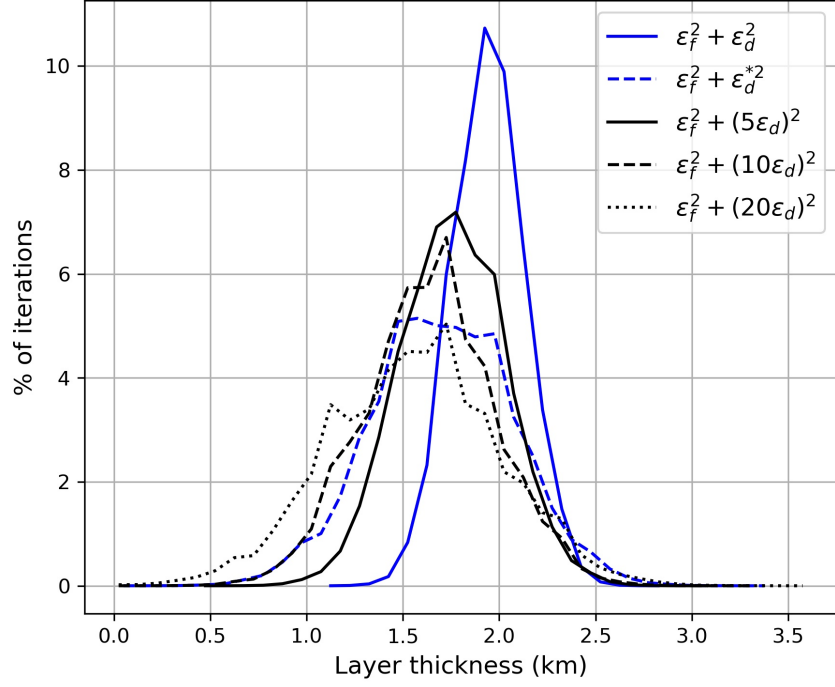


Figure S15: The results of the error propagation analysis. Curves show the distribution of the best-fitting layer thicknesses after one million iterations. Each curve is for a different denominator of the misfit function, given in the legend. ϵ_d^* indicates that the measurement errors on DKS modes only are increased by a factor of 15.875.

10 Grid search results

Figures S16, S17, and S18 show the results for the grid search procedure in greater detail. Each figure shows slices through the misfit volume where Figures S16, S17, and S18 are slices of constant P-velocity deviation, δV_p ; S-velocity deviation, δV_s ; and density deviation, $\delta\rho$, respectively - three sets of orthogonal slices through the same volume. All 729 models tested are presented and the 180 models that are excluded due to having negative bulk modules are indicated. These excluded models inhabit a poorly-fitting region of the parameter space with high δV_p and low δV_s . These results highlight the very wide parameter space that is better-fitting than no layer, making a precise assessment of layer properties impossible.

We also perform a grid search for a totally molten layer with δV_s fixed at -100% and the same intervals of δV_s and $\delta\rho$. None of the 81 models had a non-zero best-fitting thickness, reinforcing that a molten layer is not preferred over EPOC with no layer.

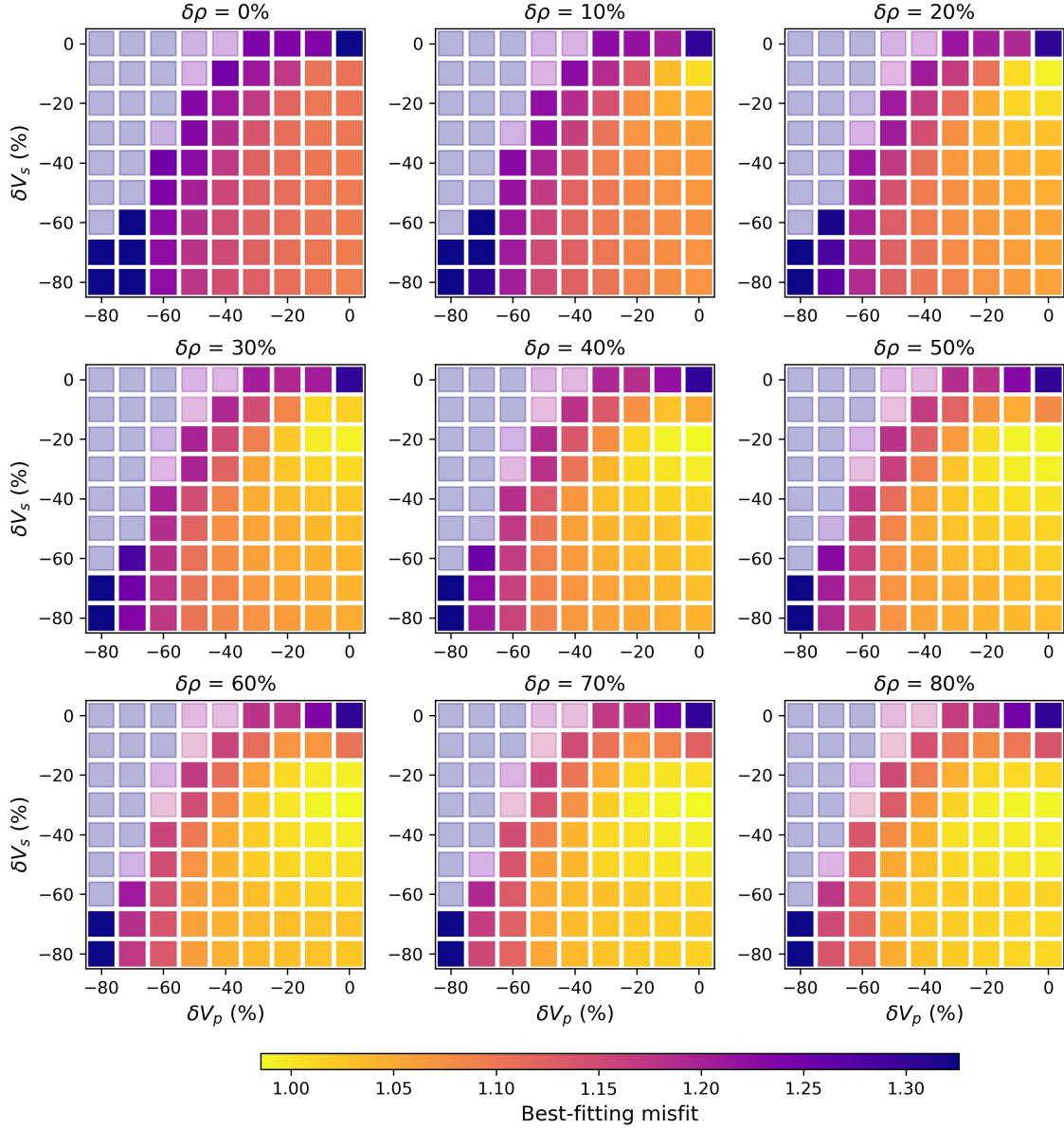


Figure S16: The best-fitting misfit as a function of δV_p and δV_s , for constant values of $\delta\rho$. Percentage deviations are relative to the lowermost mantle in PREM. Squares with high transparency represent models that are excluded as they have negative bulk modulus.

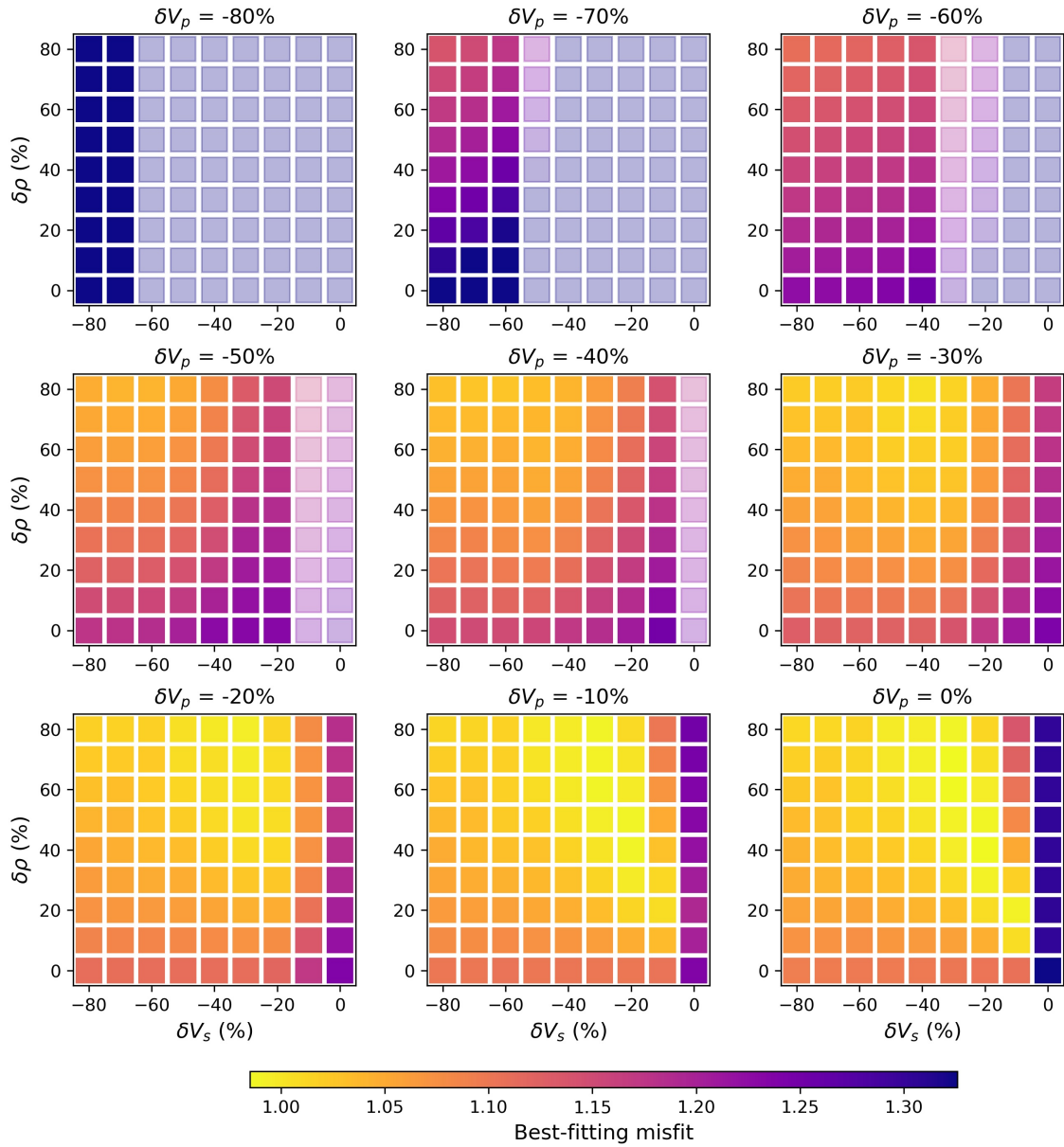


Figure S17: The best-fitting misfit as a function of δV_s and $\delta \rho$, for constant values of δV_p . Percentage deviations are relative to the lowermost mantle in PREM. Squares with high transparency represent models that are excluded as they have negative bulk modulus.

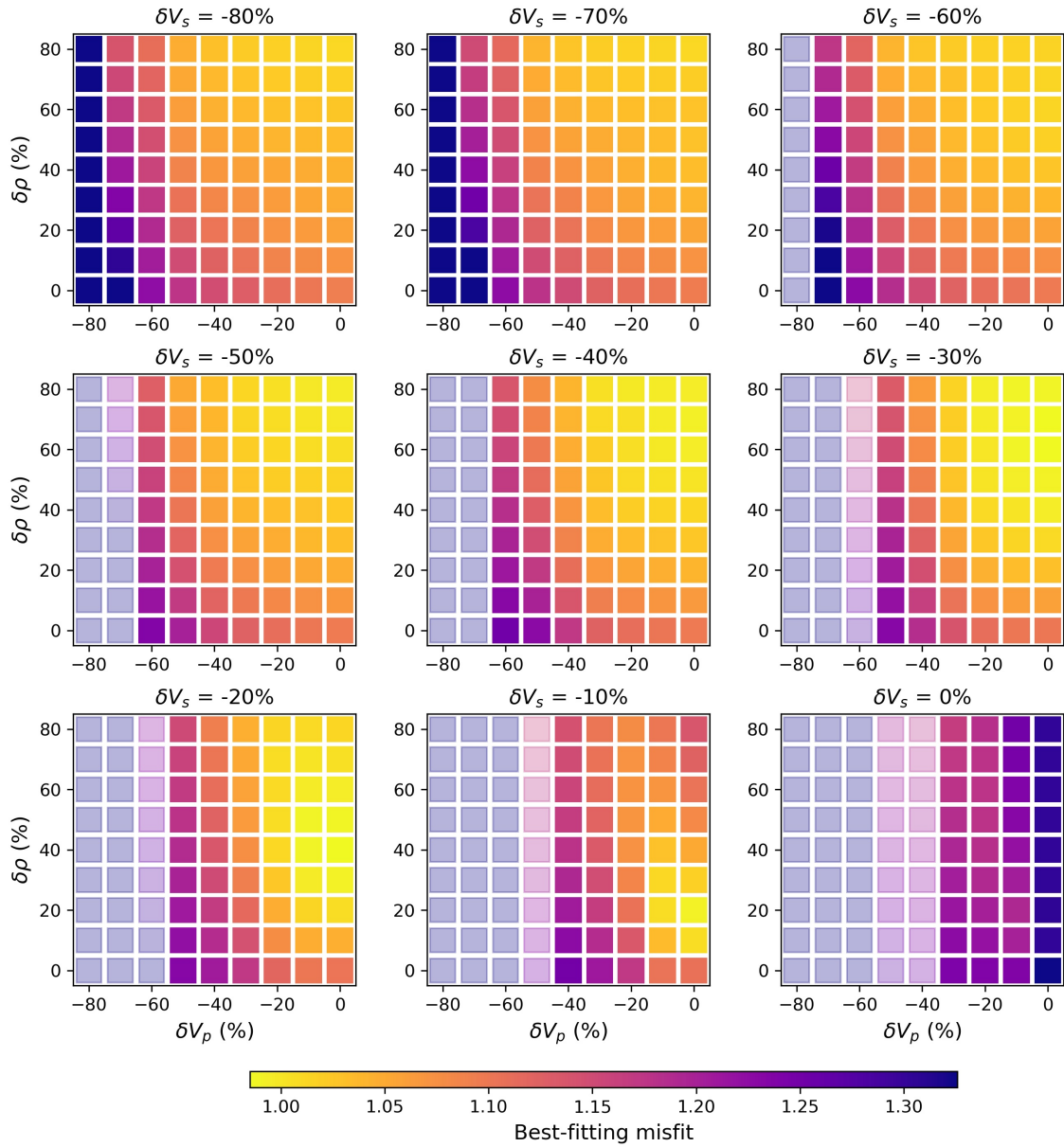


Figure S18: The best-fitting misfit as a function of δV_p and $\delta \rho$, for constant values of δV_s . Percentage deviations are relative to the lowermost mantle in PREM. Squares with high transparency represent models that are excluded as they have negative bulk modulus.

11 Mode dataset

Table S1 contains details of all 353 modes (334 spheroidal, 19 toroidal) that are included in the dataset. The centre frequencies and measurement errors are taken from the most recent study in which mode was measured (*Resovsky and Ritzwoller, 1998; Deuss et al., 2013; Koelemeijer et al., 2013; Schneider and Deuss, 2021; REM*). Note that different studies take different approaches to defining the measurement error. For the solid layer used in the main paper, the rate of change of centre frequency with layer thickness for each mode is also given in the gradient column. The measured centre frequencies are corrected for the first-order effects of ellipticity (*Dahlen and Tromp, 1998*), although this correction is minor and affects the best-fitting thickness of the solid layer by only 50 m.

Figure S19 shows the absolute rate of change of the centre frequency for different modes for the solid layer. MINEOS (*Masters et al., 2011*) calculates centre frequencies for all possible modes, however not all modes have been measured or are possible to observe. Figure S19a shows all spheroidal modes outputted by MINEOS with centre frequencies up to 10 mHz. The spheroidal modes with the greatest sensitivity are concentrated in a diagonal band across all l where n is less than 5. This band includes the strongly CMB sensitive Stoneley modes, however many of these modes at higher l values have not been measured. Figure S19b is the same but for toroidal modes with centre frequencies up to 10 mHz. The 353 modes of the dataset are shown in Figure S19c and S19d for spheroidal and toroidal modes, respectively.

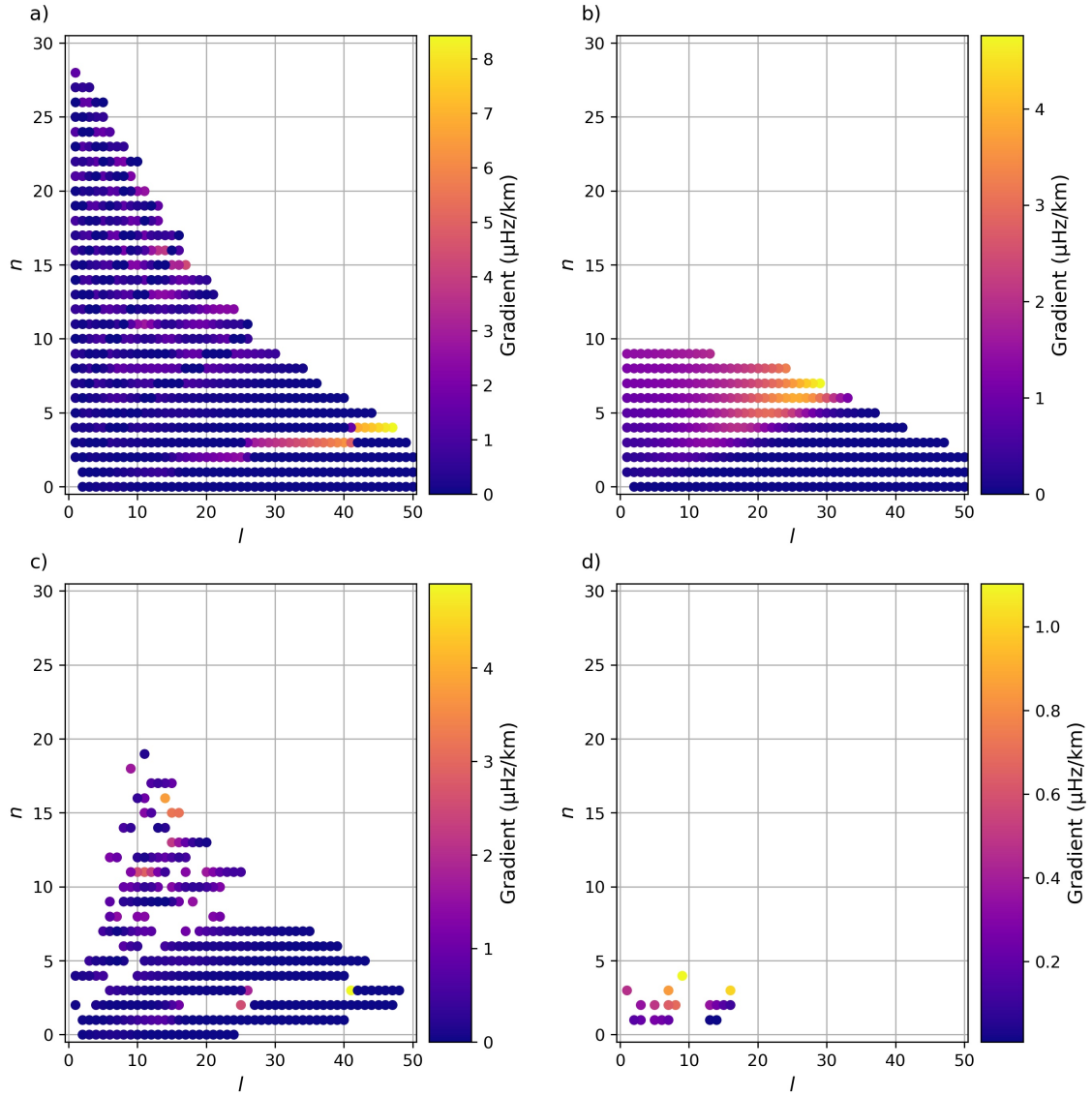


Figure S19: Absolute rate of change of centre frequency with increasing solid layer thickness plotted against n and l for (a) spheroidal modes from MINEOS, (b) toroidal modes from MINEOS, (c) the 334 spheroidal modes that are in the dataset and (d) the 19 toroidal modes that are in the dataset. Note the different colour scales for each axis.

Mode	Centre frequency (mHz)	Measurement error, ϵ_d (μ Hz)	Model error, ϵ_f (μ Hz)	Gradient (μ Hz/km)	Source
${}_0S_2$	0.30968	0.02	0.28	0.03333	D13
${}_0S_3$	0.46858	0.04	0.22	0.06759	D13
${}_0S_4$	0.64685	0.03	0.07	0.10093	D13
${}_0S_5$	0.84003	0.04	0.28	0.12679	D13
${}_0S_6$	1.03756	0.04	0.44	0.14113	D13
${}_0S_7$	1.23098	0.03	0.50	0.13806	D13
${}_0S_8$	1.41279	0.02	0.45	0.11379	D13
${}_0S_9$	1.57753	0.02	0.68	0.07650	D13
${}_0S_{10}$	1.72561	0.11	1.02	0.04357	R&R98
${}_0S_{11}$	1.86185	0.08	1.36	0.02293	D13
${}_0S_{12}$	1.98968	0.03	1.71	0.01214	D13
${}_0S_{13}$	2.11197	0.04	2.07	0.00692	D13
${}_0S_{14}$	2.23042	0.04	2.43	0.00447	D13
${}_0S_{15}$	2.34541	0.06	2.79	0.00330	D13
${}_0S_{16}$	2.45746	0.03	3.13	0.00272	D13
${}_0S_{17}$	2.56649	0.05	3.46	0.00240	D13
${}_0S_{18}$	2.67242	0.12	3.77	0.00219	R&R98
${}_0S_{19}$	2.77682	0.10	4.03	0.00203	D13
${}_0S_{20}$	2.87833	0.16	4.26	0.00190	D13
${}_0S_{21}$	2.97745	0.61	4.45	0.00178	D13
${}_0S_{22}$	3.07457	0.15	4.60	0.00168	M&W95
${}_0S_{23}$	3.17062	0.10	4.70	0.00157	M&W95
${}_0S_{24}$	3.26558	0.10	4.76	0.00148	M&W95
${}_1S_2$	0.67994	0.05	0.24	0.03920	D13
${}_1S_3$	0.94005	0.06	0.06	0.02457	D13
${}_1S_4$	1.17300	0.05	0.14	0.01992	D13
${}_1S_5$	1.37022	0.03	1.05	0.03762	D13
${}_1S_6$	1.52159	0.04	2.29	0.08397	D13
${}_1S_7$	1.65466	0.06	2.89	0.14636	D13
${}_1S_8$	1.79795	0.03	3.45	0.23406	D13
${}_1S_9$	1.96204	0.03	4.12	0.34118	D13
${}_1S_{10}$	2.14640	0.14	4.81	0.44961	D13
${}_1S_{11}$	2.34574	0.41	5.44	0.54974	K13
${}_1S_{12}$	2.55265	0.09	5.95	0.63958	K13
${}_1S_{13}$	2.76442	0.11	6.16	0.71062	K13
${}_1S_{14}$	2.97383	0.15	5.20	0.71055	K13
${}_1S_{15}$	3.16906	0.10	2.41	0.43857	K13
${}_1S_{16}$	3.33768	0.08	2.89	0.11158	K13
${}_1S_{17}$	3.49348	0.84	3.12	0.02835	REM
${}_1S_{18}$	3.64383	0.61	3.15	0.00828	REM

Table S1: Properties and composition of the modes in the dataset. Modes are ordered by n and then l with spheroidal modes followed by toroidal modes. Gradients given are for the solid layer. Sources: REM (REM), M&W95 (*Masters and Widmer, 1995*), R&R98 (*Resovsky and Ritzwoller, 1998*), D13 (*Deuss et al., 2013*), K13 (*Koelmeijer et al., 2013*), S&D21 (*Schneider and Deuss, 2021*).

Mode	Centre frequency (mHz)	Measurement error, ϵ_d (μ Hz)	Model error, ϵ_f (μ Hz)	Gradient (μ Hz/km)	Source
${}_1S_{19}$	3.79231	0.91	3.06	0.00209	REM
${}_1S_{20}$	3.94004	0.76	2.92	0.00014	REM
${}_1S_{21}$	4.08571	0.61	2.78	0.00087	REM
${}_1S_{22}$	4.23153	0.80	2.65	0.00110	REM
${}_1S_{23}$	4.37630	1.16	2.54	0.00110	REM
${}_1S_{24}$	4.52108	1.16	2.46	0.00102	REM
${}_1S_{25}$	4.66269	2.10	2.42	0.00090	REM
${}_1S_{26}$	4.80915	1.38	2.42	0.00076	REM
${}_1S_{27}$	4.95281	1.59	2.47	0.00064	REM
${}_1S_{28}$	5.08868	2.56	2.56	0.00053	REM
${}_1S_{29}$	5.23305	1.53	2.71	0.00040	REM
${}_1S_{30}$	5.37308	1.78	2.91	0.00031	REM
${}_1S_{31}$	5.51356	2.08	3.17	0.00022	REM
${}_1S_{32}$	5.65238	2.33	3.48	0.00013	REM
${}_1S_{33}$	5.78883	2.06	3.85	0.00003	REM
${}_1S_{34}$	5.92921	2.90	4.28	0.00015	REM
${}_1S_{35}$	6.06184	2.37	4.77	0.00009	REM
${}_1S_{36}$	6.19501	3.00	5.31	0.00015	REM
${}_1S_{37}$	6.33199	3.30	5.90	0.00015	REM
${}_1S_{38}$	6.46535	2.65	6.54	0.00023	REM
${}_1S_{39}$	6.59433	3.40	7.22	0.00028	REM
${}_1S_{40}$	6.72829	3.85	7.95	0.00032	REM
${}_2S_1$	0.40418	0.04	0.66	0.05505	D13
${}_2S_4$	1.37950	0.03	2.52	0.10600	D13
${}_2S_5$	1.51522	0.03	1.84	0.06976	D13
${}_2S_6$	1.68113	0.06	1.82	0.03611	D13
${}_2S_7$	1.86517	0.05	2.16	0.02241	D13
${}_2S_8$	2.04948	0.03	2.44	0.01879	D13
${}_2S_9$	2.22867	0.15	2.70	0.01953	D13
${}_2S_{10}$	2.40320	0.01	2.92	0.02348	D13
${}_2S_{11}$	2.57235	0.18	3.08	0.03175	D13
${}_2S_{12}$	2.73726	0.02	3.13	0.04822	D13
${}_2S_{13}$	2.89989	0.04	3.00	0.08586	D13
${}_2S_{14}$	3.06236	0.07	2.30	0.19969	K13
${}_2S_{15}$	3.23880	0.03	4.90	0.59212	K13
${}_2S_{16}$	3.44091	0.14	8.90	1.04683	K13
${}_2S_{25}$	5.39732	0.20	15.52	2.55813	K13
${}_2S_{27}$	5.74614	0.85	4.08	0.02412	REM
${}_2S_{28}$	5.90383	1.10	4.32	0.00368	REM
${}_2S_{29}$	6.06816	1.28	4.56	0.00077	REM

Table S1: Continued: properties and composition of the modes in the dataset. Modes are ordered by n and then l with spheroidal modes followed by toroidal modes. Gradients given are for the solid layer. Sources: REM (REM), M&W95 (*Masters and Widmer*, 1995), R&R98 (*Resovsky and Ritzwoller*, 1998), D13 (*Deuss et al.*, 2013), K13 (*Koelemeijer et al.*, 2013), S&D21 (*Schneider and Deuss*, 2021).

Mode	Centre frequency (mHz)	Measurement error, ϵ_d (μ Hz)	Model error, ϵ_f (μ Hz)	Gradient (μ Hz/km)	Source
${}_2S_{30}$	6.22858	1.17	4.79	0.00000	REM
${}_2S_{31}$	6.38518	1.13	5.02	0.00025	REM
${}_2S_{32}$	6.54111	1.49	5.25	0.00036	REM
${}_2S_{33}$	6.69721	1.34	5.48	0.00042	REM
${}_2S_{34}$	6.85210	1.25	5.70	0.00045	REM
${}_2S_{35}$	7.01193	2.31	5.91	0.00046	REM
${}_2S_{36}$	7.16443	2.45	6.12	0.00047	REM
${}_2S_{37}$	7.31857	2.07	6.31	0.00047	REM
${}_2S_{38}$	7.47302	1.81	6.49	0.00049	REM
${}_2S_{39}$	7.62341	2.66	6.64	0.00046	REM
${}_2S_{40}$	7.77496	2.50	6.78	0.00046	REM
${}_2S_{41}$	7.92126	3.89	6.88	0.00044	REM
${}_2S_{42}$	8.06990	4.58	6.96	0.00041	REM
${}_2S_{43}$	8.21956	4.06	7.01	0.00040	REM
${}_2S_{44}$	8.36056	4.24	7.02	0.00038	REM
${}_2S_{45}$	8.50898	4.44	7.00	0.00034	REM
${}_2S_{46}$	8.65704	4.73	6.95	0.00032	REM
${}_2S_{47}$	8.80729	5.10	6.86	0.00028	REM
${}_3S_6$	2.54880	0.08	2.33	0.43663	D13
${}_3S_7$	2.68577	0.21	2.22	0.35142	D13
${}_3S_8$	2.81924	0.03	2.02	0.26385	D13
${}_3S_9$	2.95137	0.03	1.76	0.19130	D13
${}_3S_{10}$	3.08210	0.50	1.51	0.13793	REM
${}_3S_{11}$	3.21950	0.53	1.27	0.10097	REM
${}_3S_{12}$	3.36134	0.41	1.06	0.07605	REM
${}_3S_{13}$	3.50753	0.55	1.15	0.05938	REM
${}_3S_{14}$	3.65618	0.53	1.35	0.04793	REM
${}_3S_{15}$	3.81096	0.59	1.56	0.03975	REM
${}_3S_{16}$	3.96683	0.65	1.76	0.03368	REM
${}_3S_{17}$	4.12400	0.60	1.97	0.02899	REM
${}_3S_{18}$	4.28379	0.67	2.17	0.02534	REM
${}_3S_{19}$	4.44612	0.67	2.38	0.02255	REM
${}_3S_{20}$	4.60897	0.88	2.59	0.02058	REM
${}_3S_{21}$	4.77158	0.75	2.79	0.01955	REM
${}_3S_{22}$	4.93287	0.85	3.00	0.01987	REM
${}_3S_{23}$	5.09842	0.76	3.19	0.02270	REM
${}_3S_{24}$	5.26295	0.81	3.34	0.03278	REM
${}_3S_{25}$	5.42711	0.15	2.73	0.08664	K13
${}_3S_{26}$	5.62085	0.24	17.54	1.80030	K13
${}_3S_{41}$	8.82312	2.57	1.82	4.90257	REM

Table S1: Continued: properties and composition of the modes in the dataset. Modes are ordered by n and then l with spheroidal modes followed by toroidal modes. Gradients given are for the solid layer. Sources: REM (REM), M&W95 (*Masters and Widmer*, 1995), R&R98 (*Resovsky and Ritzwoller*, 1998), D13 (*Deuss et al.*, 2013), K13 (*Koelemeijer et al.*, 2013), S&D21 (*Schneider and Deuss*, 2021).

Mode	Centre frequency (mHz)	Measurement error, ϵ_d (μ Hz)	Model error, ϵ_f (μ Hz)	Gradient (μ Hz/km)	Source
${}_3S_{42}$	8.97689	2.41	1.36	0.00091	REM
${}_3S_{43}$	9.13826	2.30	0.87	0.00021	REM
${}_3S_{44}$	9.29013	2.43	0.34	0.00002	REM
${}_3S_{45}$	9.44223	3.31	0.23	0.00015	REM
${}_3S_{46}$	9.60346	2.47	0.83	0.00000	REM
${}_3S_{47}$	9.75065	2.46	1.48	0.00000	REM
${}_3S_{48}$	9.90813	3.93	2.16	0.00011	REM
${}_4S_1$	1.41179	0.05	0.40	0.13150	D13
${}_4S_2$	1.72140	0.05	0.51	0.14143	D13
${}_4S_3$	2.04827	0.01	0.39	0.16655	D13
${}_4S_4$	2.27830	0.03	1.65	0.49031	D13
${}_4S_5$	2.41112	0.03	2.17	0.49078	D13
${}_4S_{10}$	3.86407	0.63	2.40	0.41341	REM
${}_4S_{11}$	4.00750	1.00	2.55	0.38606	REM
${}_4S_{12}$	4.15199	1.50	2.56	0.32587	REM
${}_4S_{13}$	4.29204	1.04	2.51	0.26169	REM
${}_4S_{14}$	4.43529	0.81	2.47	0.20459	REM
${}_4S_{15}$	4.58399	1.50	2.44	0.15788	REM
${}_4S_{16}$	4.72984	1.50	2.44	0.12105	REM
${}_4S_{17}$	4.88531	1.14	2.46	0.09255	REM
${}_4S_{18}$	5.04365	1.05	2.51	0.07067	REM
${}_4S_{19}$	5.20062	1.53	2.58	0.05392	REM
${}_4S_{20}$	5.36218	1.26	2.67	0.04110	REM
${}_4S_{21}$	5.52606	1.29	2.78	0.03127	REM
${}_4S_{22}$	5.69499	1.50	2.90	0.02374	REM
${}_4S_{23}$	5.86147	1.34	3.03	0.01798	REM
${}_4S_{24}$	6.02866	1.49	3.16	0.01360	REM
${}_4S_{25}$	6.19722	1.58	3.30	0.01027	REM
${}_4S_{26}$	6.36548	1.24	3.43	0.00775	REM
${}_4S_{27}$	6.53553	1.73	3.56	0.00589	REM
${}_4S_{28}$	6.70264	1.86	3.67	0.00447	REM
${}_4S_{29}$	6.87294	1.30	3.76	0.00343	REM
${}_4S_{30}$	7.03810	1.30	3.83	0.00266	REM
${}_4S_{31}$	7.20440	2.12	3.86	0.00209	REM
${}_4S_{32}$	7.36938	1.58	3.87	0.00167	REM
${}_4S_{33}$	7.53650	1.87	3.83	0.00136	REM
${}_4S_{34}$	7.70007	1.83	3.74	0.00113	REM
${}_4S_{35}$	7.85957	1.78	3.61	0.00096	REM
${}_4S_{36}$	8.01994	1.48	3.43	0.00083	REM
${}_4S_{37}$	8.18437	1.48	3.21	0.00074	REM

Table S1: Continued: properties and composition of the modes in the dataset. Modes are ordered by n and then l with spheroidal modes followed by toroidal modes. Gradients given are for the solid layer. Sources: REM (REM), M&W95 (*Masters and Widmer*, 1995), R&R98 (*Resovsky and Ritzwoller*, 1998), D13 (*Deuss et al.*, 2013), K13 (*Koelemeijer et al.*, 2013), S&D21 (*Schneider and Deuss*, 2021).

Mode	Centre frequency (mHz)	Measurement error, ϵ_d (μ Hz)	Model error, ϵ_f (μ Hz)	Gradient (μ Hz/km)	Source
${}_4S_{38}$	8.34214	2.15	2.93	0.00069	REM
${}_4S_{39}$	8.49951	2.34	2.60	0.00072	REM
${}_4S_{40}$	8.66348	2.81	2.28	0.00110	REM
${}_5S_3$	2.16868	0.06	0.98	0.39228	D13
${}_5S_4$	2.37918	0.04	0.30	0.14146	D13
${}_5S_5$	2.70340	0.01	0.27	0.11232	D13
${}_5S_6$	3.01105	0.05	0.43	0.04457	D13
${}_5S_7$	3.29165	0.04	0.53	0.00336	D13
${}_5S_8$	3.52593	0.02	1.09	0.12761	D13
${}_5S_{11}$	4.45688	0.11	0.44	0.24028	D13
${}_5S_{12}$	4.69577	0.03	0.49	0.22440	D13
${}_5S_{13}$	4.92550	1.02	0.65	0.24944	REM
${}_5S_{14}$	5.13496	0.06	1.60	0.30165	D13
${}_5S_{15}$	5.32687	0.02	2.75	0.34504	D13
${}_5S_{16}$	5.50245	0.10	3.64	0.34787	D13
${}_5S_{17}$	5.66876	0.06	4.13	0.31599	D13
${}_5S_{18}$	5.82920	1.96	4.35	0.26906	REM
${}_5S_{19}$	5.98849	2.17	4.42	0.22024	REM
${}_5S_{20}$	6.15222	1.88	4.39	0.17555	REM
${}_5S_{21}$	6.31038	2.18	4.30	0.13712	REM
${}_5S_{22}$	6.47356	1.85	4.15	0.10525	REM
${}_5S_{23}$	6.63542	1.79	3.94	0.07951	REM
${}_5S_{24}$	6.80077	2.32	3.66	0.05914	REM
${}_5S_{25}$	6.96593	1.92	3.30	0.04333	REM
${}_5S_{26}$	7.13265	1.79	2.86	0.03130	REM
${}_5S_{27}$	7.29192	2.22	2.31	0.02232	REM
${}_5S_{28}$	7.45535	2.08	1.67	0.01575	REM
${}_5S_{29}$	7.61687	2.41	0.95	0.01102	REM
${}_5S_{30}$	7.77851	2.60	0.14	0.00769	REM
${}_5S_{31}$	7.94177	2.35	0.78	0.00537	REM
${}_5S_{32}$	8.09905	2.06	1.65	0.00377	REM
${}_5S_{33}$	8.25358	2.54	2.52	0.00268	REM
${}_5S_{34}$	8.40899	4.00	3.36	0.00195	REM
${}_5S_{35}$	8.57058	2.82	4.14	0.00145	REM
${}_5S_{36}$	8.72694	3.44	4.84	0.00111	REM
${}_5S_{37}$	8.88449	2.89	5.43	0.00089	REM
${}_5S_{38}$	9.04366	2.70	5.91	0.00074	REM
${}_5S_{39}$	9.20062	3.12	6.25	0.00062	REM
${}_5S_{40}$	9.36048	3.77	6.46	0.00055	REM
${}_5S_{41}$	9.50999	5.00	6.54	0.00048	REM

Table S1: Continued: properties and composition of the modes in the dataset. Modes are ordered by n and then l with spheroidal modes followed by toroidal modes. Gradients given are for the solid layer. Sources: REM (REM), M&W95 (*Masters and Widmer*, 1995), R&R98 (*Resovsky and Ritzwoller*, 1998), D13 (*Deuss et al.*, 2013), K13 (*Koelemeijer et al.*, 2013), S&D21 (*Schneider and Deuss*, 2021).

Mode	Centre frequency (mHz)	Measurement error, ϵ_d (μ Hz)	Model error, ϵ_f (μ Hz)	Gradient (μ Hz/km)	Source
${}_5S_{42}$	9.67931	3.10	6.49	0.00046	REM
${}_5S_{43}$	9.83576	4.64	6.32	0.00042	REM
${}_6S_8$	3.73751	2.00	2.11	0.76092	REM
${}_6S_9$	3.96501	0.04	0.96	0.47702	D13
${}_6S_{10}$	4.21105	0.03	0.53	0.31143	D13
${}_6S_{14}$	5.41101	2.00	1.70	0.50727	REM
${}_6S_{15}$	5.60125	0.13	2.69	0.35179	D13
${}_6S_{16}$	5.80677	1.33	4.01	0.24289	REM
${}_6S_{17}$	6.02074	1.13	5.13	0.18121	REM
${}_6S_{18}$	6.23570	0.08	6.09	0.14973	D13
${}_6S_{19}$	6.44619	1.76	6.90	0.13545	REM
${}_6S_{20}$	6.65393	1.31	7.54	0.13072	REM
${}_6S_{21}$	6.85524	1.80	7.96	0.13039	REM
${}_6S_{22}$	7.05035	1.64	8.14	0.12996	REM
${}_6S_{23}$	7.23478	1.48	8.13	0.12588	REM
${}_6S_{24}$	7.41252	2.08	8.03	0.11666	REM
${}_6S_{25}$	7.58815	2.01	7.93	0.10305	REM
${}_6S_{26}$	7.75615	2.10	7.87	0.08710	REM
${}_6S_{27}$	7.92195	1.63	7.85	0.07089	REM
${}_6S_{28}$	8.08819	2.04	7.85	0.05593	REM
${}_6S_{29}$	8.25579	2.03	7.82	0.04297	REM
${}_6S_{30}$	8.41722	3.07	7.74	0.03225	REM
${}_6S_{31}$	8.58831	2.65	7.56	0.02374	REM
${}_6S_{32}$	8.75932	3.13	7.27	0.01717	REM
${}_6S_{33}$	8.92692	2.62	6.87	0.01222	REM
${}_6S_{34}$	9.09208	2.92	6.34	0.00860	REM
${}_6S_{35}$	9.25799	3.61	5.70	0.00596	REM
${}_6S_{36}$	9.42384	3.10	4.93	0.00411	REM
${}_6S_{37}$	9.59800	3.50	4.06	0.00282	REM
${}_6S_{38}$	9.76062	2.89	3.08	0.00193	REM
${}_6S_{39}$	9.92885	2.27	2.02	0.00132	REM
${}_7S_5$	3.65753	0.02	1.95	0.53110	D13
${}_7S_6$	3.95562	0.02	2.99	0.23759	D13
${}_7S_7$	4.23437	0.03	3.81	0.04431	D13
${}_7S_8$	4.44941	0.13	4.05	0.21890	D13
${}_7S_9$	4.61444	0.14	3.95	0.53275	D13
${}_7S_{10}$	4.76350	4.50	3.81	0.73377	REM
${}_7S_{11}$	4.91550	3.00	3.55	0.80700	REM
${}_7S_{12}$	5.06925	1.53	3.01	0.77668	REM
${}_7S_{17}$	6.61015	3.77	3.32	1.07422	REM

Table S1: Continued: properties and composition of the modes in the dataset. Modes are ordered by n and then l with spheroidal modes followed by toroidal modes. Gradients given are for the solid layer. Sources: REM (REM), M&W95 (*Masters and Widmer*, 1995), R&R98 (*Resovsky and Ritzwoller*, 1998), D13 (*Deuss et al.*, 2013), K13 (*Koelemeijer et al.*, 2013), S&D21 (*Schneider and Deuss*, 2021).

Mode	Centre frequency (mHz)	Measurement error, ϵ_d (μ Hz)	Model error, ϵ_f (μ Hz)	Gradient (μ Hz/km)	Source
$7S_{19}$	6.91981	4.48	2.05	0.76908	REM
$7S_{20}$	7.07702	3.61	1.73	0.62624	REM
$7S_{21}$	7.24837	2.82	2.23	0.49808	REM
$7S_{22}$	7.41874	1.96	3.60	0.38848	REM
$7S_{23}$	7.59393	1.68	5.16	0.29956	REM
$7S_{24}$	7.77889	2.24	6.75	0.23104	REM
$7S_{25}$	7.96279	1.87	8.23	0.18010	REM
$7S_{26}$	8.15435	2.26	9.48	0.14265	REM
$7S_{27}$	8.34233	1.70	10.44	0.11479	REM
$7S_{28}$	8.52134	4.00	11.08	0.09339	REM
$7S_{29}$	8.70931	4.00	11.42	0.07632	REM
$7S_{30}$	8.90255	2.35	11.48	0.06221	REM
$7S_{31}$	9.08932	2.74	11.27	0.05030	REM
$7S_{32}$	9.27918	2.30	10.85	0.04015	REM
$7S_{33}$	9.45748	2.07	10.26	0.03154	REM
$7S_{34}$	9.63685	2.67	9.54	0.02435	REM
$7S_{35}$	9.82031	2.70	8.72	0.01844	REM
$8S_6$	4.43029	0.03	1.94	0.80539	D13
$8S_7$	4.64644	0.16	0.41	1.45558	D13
$8S_{10}$	5.50302	0.04	1.62	1.28788	D13
$8S_{11}$	5.70954	1.44	5.13	1.32650	REM
$8S_{21}$	7.97633	4.25	3.66	1.24481	REM
$8S_{22}$	8.12786	4.39	3.08	1.09539	REM
$9S_6$	4.61887	0.17	3.26	0.81608	D13
$9S_8$	5.13846	0.06	7.26	0.26303	D13
$9S_9$	5.38154	3.00	7.07	0.22732	REM
$9S_{10}$	5.60608	0.23	4.97	0.08747	D13
$9S_{11}$	5.88236	0.05	2.61	0.07572	D13
$9S_{12}$	6.18367	0.04	2.60	0.05106	D13
$9S_{13}$	6.48069	0.05	2.42	0.00705	D13
$9S_{14}$	6.76472	0.03	1.77	0.01260	D13
$9S_{15}$	7.02530	0.10	1.57	0.28308	D13
$9S_{16}$	7.23273	2.51	5.14	1.02915	REM
$9S_{18}$	7.54147	3.86	5.30	1.52990	REM
$10S_8$	5.73500	7.00	3.46	0.95393	REM
$10S_9$	5.93899	4.50	5.45	0.97559	REM
$10S_{10}$	6.18646	0.21	8.12	0.67123	D13
$10S_{11}$	6.44665	2.06	9.68	0.33502	REM
$10S_{12}$	6.68499	4.00	8.81	0.45791	REM
$10S_{13}$	6.86378	2.85	6.82	0.96844	REM

Table S1: Continued: properties and composition of the modes in the dataset. Modes are ordered by n and then l with spheroidal modes followed by toroidal modes. Gradients given are for the solid layer. Sources: REM (REM), M&W95 (*Masters and Widmer*, 1995), R&R98 (*Resovsky and Ritzwoller*, 1998), D13 (*Deuss et al.*, 2013), K13 (*Koelemeijer et al.*, 2013), S&D21 (*Schneider and Deuss*, 2021).

Mode	Centre frequency (mHz)	Measurement error, ϵ_d (μ Hz)	Model error, ϵ_f (μ Hz)	Gradient (μ Hz/km)	Source
$_{10}S_{15}$	7.19800	5.00	3.72	1.37551	REM
$_{10}S_{16}$	7.42013	1.52	5.79	0.77048	REM
$_{10}S_{17}$	7.67267	0.07	5.88	0.41226	D13
$_{10}S_{18}$	7.93640	0.11	5.49	0.31037	D13
$_{10}S_{19}$	8.19677	0.09	4.89	0.33182	D13
$_{10}S_{20}$	8.44607	0.16	3.84	0.49206	D13
$_{10}S_{21}$	8.67134	0.18	2.03	0.85577	D13
$_{10}S_{22}$	8.86468	2.44	2.25	1.24961	REM
$_{11}S_9$	6.43187	0.05	2.03	1.28565	D13
$_{11}S_{10}$	6.70557	0.11	2.03	2.52129	D13
$_{11}S_{11}$	6.91500	9.00	3.98	2.88715	REM
$_{11}S_{12}$	7.14296	0.41	7.83	2.24189	D13
$_{11}S_{13}$	7.41149	4.00	11.79	1.18150	REM
$_{11}S_{14}$	7.67954	0.52	13.54	0.42144	D13
$_{11}S_{17}$	8.26500	8.00	8.28	1.34157	REM
$_{11}S_{20}$	8.72419	4.78	3.89	1.65628	REM
$_{11}S_{21}$	8.89697	3.35	2.81	1.28358	REM
$_{11}S_{22}$	9.10307	2.35	3.60	0.83235	REM
$_{11}S_{23}$	9.33287	0.25	4.27	0.58032	D13
$_{11}S_{24}$	9.57049	0.24	4.19	0.50042	D13
$_{11}S_{25}$	9.80853	0.13	3.75	0.52349	D13
$_{12}S_6$	5.64385	0.15	3.37	1.23691	D13
$_{12}S_7$	5.85244	0.10	2.60	0.98075	D13
$_{12}S_{10}$	6.85999	5.00	5.20	0.25527	REM
$_{12}S_{11}$	7.13344	0.04	5.35	0.13445	D13
$_{12}S_{12}$	7.44891	0.04	4.39	0.44311	D13
$_{12}S_{13}$	7.76984	0.11	3.31	0.72567	D13
$_{12}S_{14}$	8.09028	0.09	2.31	0.90544	D13
$_{12}S_{15}$	8.40452	0.09	3.22	0.59477	D13
$_{12}S_{16}$	8.68669	0.11	11.50	0.36440	D13
$_{12}S_{17}$	8.92822	0.14	13.35	0.52073	D13
$_{13}S_{15}$	8.47266	0.63	10.65	2.21679	D13
$_{13}S_{16}$	8.74485	0.28	3.96	1.59814	D13
$_{13}S_{17}$	9.05382	1.56	3.24	0.88172	REM
$_{13}S_{18}$	9.36372	0.11	3.19	0.39762	D13
$_{13}S_{19}$	9.66449	0.14	2.98	0.13947	D13
$_{13}S_{20}$	9.95448	0.10	3.01	0.07145	D13
$_{14}S_8$	7.04253	0.28	4.33	0.58137	D13
$_{14}S_9$	7.34452	0.12	5.65	0.35213	D13
$_{14}S_{13}$	8.72982	0.07	7.88	0.10955	D13

Table S1: Continued: properties and composition of the modes in the dataset. Modes are ordered by n and then l with spheroidal modes followed by toroidal modes. Gradients given are for the solid layer. Sources: REM (REM), M&W95 (*Masters and Widmer*, 1995), R&R98 (*Resovsky and Ritzwoller*, 1998), D13 (*Deuss et al.*, 2013), K13 (*Koelemeijer et al.*, 2013), S&D21 (*Schneider and Deuss*, 2021).

Mode	Centre frequency (mHz)	Measurement error, ϵ_d (μ Hz)	Model error, ϵ_f (μ Hz)	Gradient (μ Hz/km)	Source
$_{14}\text{S}_{14}$	8.98149	0.08	7.93	0.23474	D13
$_{15}\text{S}_{11}$	8.12241	1.50	6.10	1.35115	REM
$_{15}\text{S}_{12}$	8.42773	0.13	7.15	0.63755	D13
$_{15}\text{S}_{15}$	9.59215	0.11	3.39	3.22890	D13
$_{15}\text{S}_{16}$	9.92112	0.16	2.16	3.16762	D13
$_{16}\text{S}_{10}$	8.43336	0.08	5.47	0.35160	D13
$_{16}\text{S}_{11}$	8.73013	0.27	5.76	1.04709	D13
$_{16}\text{S}_{14}$	9.29932	0.95	3.28	3.80556	D13
$_{17}\text{S}_{12}$	9.14844	0.06	7.25	0.67647	D13
$_{17}\text{S}_{13}$	9.42847	0.08	9.13	0.47829	D13
$_{17}\text{S}_{14}$	9.69854	0.30	9.30	0.60608	D13
$_{17}\text{S}_{15}$	9.93267	0.52	8.21	0.93383	D13
$_{18}\text{S}_9$	8.73500	7.00	5.91	1.66112	REM
$_{19}\text{S}_{11}$	9.64479	0.23	5.65	0.16856	D13
$_1\text{T}_2$	1.31929	0.17	0.46	0.17728	S&D21
$_1\text{T}_3$	1.43845	0.08	0.48	0.22153	S&D21
$_1\text{T}_5$	1.75019	0.13	0.57	0.26744	S&D21
$_1\text{T}_6$	1.92525	0.12	0.62	0.25168	S&D21
$_1\text{T}_7$	2.10340	0.06	0.67	0.21273	S&D21
$_1\text{T}_{13}$	3.09907	0.10	0.86	0.01422	S&D21
$_1\text{T}_{14}$	3.25352	0.06	0.82	0.00776	S&D21
$_2\text{T}_3$	2.29528	0.22	0.33	0.35163	S&D21
$_2\text{T}_5$	2.48487	0.15	0.69	0.49077	S&D21
$_2\text{T}_7$	2.75300	0.33	1.14	0.64240	S&D21
$_2\text{T}_8$	2.91257	0.08	1.36	0.68896	S&D21
$_2\text{T}_{13}$	3.83052	0.21	1.69	0.35745	S&D21
$_2\text{T}_{14}$	4.01381	0.24	1.56	0.25537	S&D21
$_2\text{T}_{15}$	4.19269	0.22	1.37	0.17272	S&D21
$_2\text{T}_{16}$	4.36875	0.53	1.13	0.11167	S&D21
$_3\text{T}_1$	3.20008	1.73	1.86	0.46639	S&D21
$_3\text{T}_7$	3.60368	0.24	1.84	0.84837	S&D21
$_3\text{T}_{16}$	5.05139	0.23	0.65	1.00943	S&D21
$_4\text{T}_9$	4.77537	1.86	0.11	1.10294	S&D21

Table S1: Continued: properties and composition of the modes in the dataset. Modes are ordered by n and then l with spheroidal modes followed by toroidal modes. Gradients given are for the solid layer. Sources: REM (REM), M&W95 (*Masters and Widmer, 1995*), R&R98 (*Resovsky and Ritzwoller, 1998*), D13 (*Deuss et al., 2013*), K13 (*Koelemeijer et al., 2013*), S&D21 (*Schneider and Deuss, 2021*).

References

- Akbarashrafi, F., D. Al-Attar, A. Deuss, J. Trampert, and A. Valentine, Exact free oscillation spectra, splitting functions and the resolvability of Earth's density structure, *Geophysical Journal International*, *213*(1), 58–76, doi:10.1093/gji/ggx539, 2018.
- Dahlen, F. A., and J. Tromp, *Theoretical Global Seismology*, Princeton University Press, 1998.
- De Wit, R., and J. Trampert, Robust constraints on average radial lower mantle anisotropy and consequences for composition and texture, *Earth and Planetary Science Letters*, *429*, 101–109, doi:10.1016/j.epsl.2015.07.057, 2015.
- Deuss, A., J. Ritsema, and H. van Heijst, A new catalogue of normal-mode splitting function measurements up to 10 mHz, *Geophysical Journal International*, *193*(2), 920–937, doi:10.1093/gji/ggt010, 2013.
- Dziewonski, A. M., and D. Anderson, Preliminary Reference Earth Model, *Phys. Earth Planet. Inter.*, *25*(4), 297–356, doi:10.1016/0031-9201(81)90046-7, 1981.
- Irving, J. C. E., S. Cottar, and V. Lekić, Seismically determined elastic parameters for Earth's outer core, *Science Advances*, *4*(6), eaar2538, doi:10.1126/sciadv.aar2538, 2018.
- Kennett, B. L., E. Engdahl, and R. Buland, Constraints on seismic velocities in the Earth from traveltimes, *Geophysical Journal International*, *122*(1), 108–124, doi:10.1111/j.1365-246X.1995.tb03540.x, 1995.
- Koelemeijer, P., A. Deuss, and J. Ritsema, Observations of core-mantle boundary Stoneley modes, *Geophysical Research Letters*, *40*(11), 2557–2561, doi:10.1002/grl.50514, 2013.
- Kustowski, B., G. Ekström, and A. M. Dziewoński, Anisotropic shear-wave velocity structure of the Earth's mantle: A global model, *Journal of Geophysical Research: Solid Earth*, *113*(B6), doi:10.1029/2007JB005169, 2008.
- Masters, G., and R. Widmer, Free oscillations: frequencies and attenuations, *Global Earth Physics: a handbook of physical constants*, *1*, 104, 1995.
- Masters, G., M. Barmine, and S. Kientz, *Mineos*, California Institute of Technology, Pasadena, CA, 2011.
- Montagner, J.-P., and B. Kennett, How to reconcile body-wave and normal-mode reference Earth models, *Geophysical Journal International*, *125*(1), 229–248, doi:10.1111/j.1365-246X.1996.tb06548.x, 1996.
- REM, Reference Earth Model, https://igppweb.ucsd.edu/~gabi/rem.dir/surface/rem_surf.html, accessed: 2022-11-07.
- Resovsky, J. S., and M. H. Ritzwoller, New and refined constraints on three-dimensional Earth structure from normal modes below 3 mHz, *Journal of Geophysical Research: Solid Earth*, *103*(B1), 783–810, doi:10.1029/97JB02482, 1998.
- Schneider, S., and A. Deuss, A new catalogue of toroidal-mode overtone splitting function measurements, *Geophysical Journal International*, *225*(1), 329–341, doi:10.1093/gji/ggaa567, 2021.
- Stoneley, R., Elastic waves at the surface of separation of two solids, *Proceedings of the Royal Society of London. Series A, Containing Papers of a Mathematical and Physical Character*, *106*(738), 416–428, doi:10.1098/rspa.1924.0079, 1924.